Matter

CellPress

Article

Strong fatigue-resistant nanofibrous hydrogels inspired by lobster underbelly

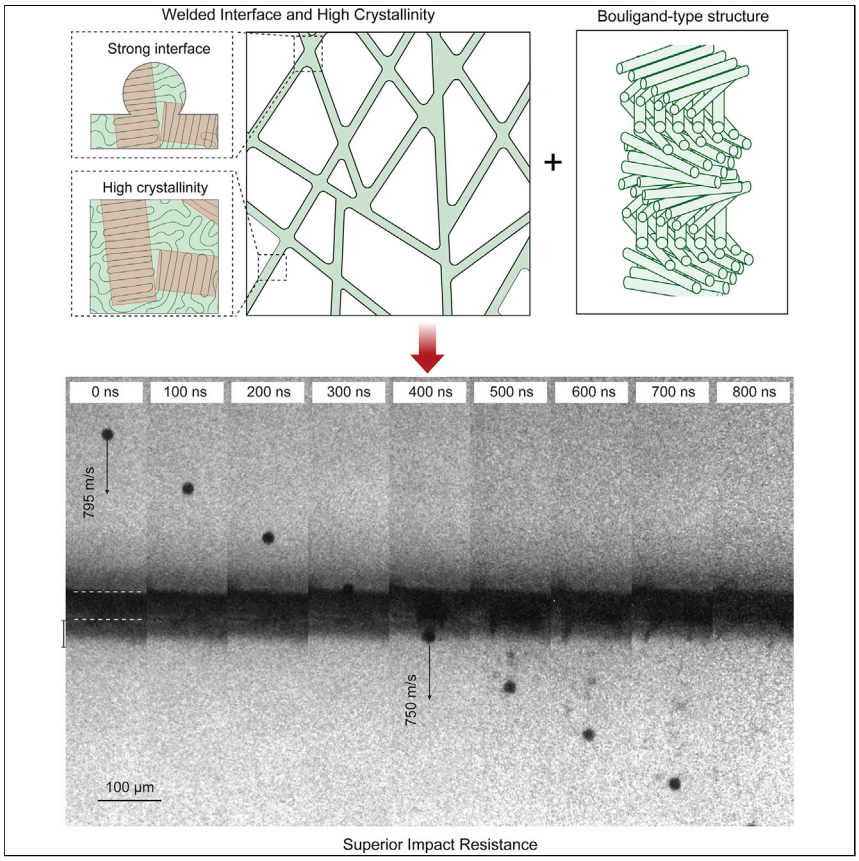

Fatigue-resistant properties have not been explored and achieved in nanofibrous hydrogels. Here, we report a bioinspired design of strong and fatigue-resistant nanofibrous hydrogels through the hierarchical assembly of a bouligand-type, welded, and high-crystalline fibril structure. The resultant nanofibrous hydrogels show superior impact resistance, suggesting potential as the next-generation flexible protective fabric.

Jiahua Ni, Shaoting Lin, Zhao Qin, ..., Raul Radovitzky, Keith A. Nelson, Xuanhe Zhao

zhaox@mit.edu

Highlights

Hierarchical assembly of welded and high-crystalline bouligand structure in hydrogels

Mechanics-guided design of high fatigue resistance for nanofibrous hydrogels

Fatigue characterization of nanofibers in synthetic hydrogels

High-velocity microparticle impacts on synthetic nanofibrous hydrogels

5 **Improvement**
Enhanced performance with innovative design or material control

Ni et al., Matter 4, 1919–1934
June 2, 2021 © 2021 Elsevier Inc.
https://doi.org/10.1016/j.matt.2021.03.023

Matter

CellPress

Article

Strong fatigue-resistant nanofibrous hydrogels inspired by lobster underbelly

Jiahua Ni,[1,9] Shaoting Lin,[1,9] Zhao Qin,[2,9] David Veysset,[3,4,5] Xinyue Liu,[1] Yuchen Sun,[3,4] Alex J. Hsieh,[6] Raul Radovitzky,[3,7] Keith A. Nelson,[3,4] and Xuanhe Zhao[1,8,10,*]

SUMMARY

Nanofibrous hydrogels are pervasive in animal and plant bodies and have been widely seen in engineering applications. Electrospinning is one of the most widely used methods for the fabrication of nanofibrous hydrogels. Whereas the biological nanofibrous hydrogels can maintain high strength and high toughness under multiple cycles of mechanical loads, such fatigue-resistant properties have not been achieved in electrospun nanofibrous hydrogels. Here, we report a bioinspired design of strong and fatigue-resistant nanofibrous hydrogels that can closely mimic the bouligand structure of the natural hydrogel in the lobster underbelly. The resultant nanofibrous hydrogel can reach high nominal strength up to 8.4 MPa and high fatigue threshold up to 770 J/m^2. We further demonstrate the superior impact resistance of the bioinspired bouligand-type nanofibrous hydrogel with specific penetration energy of 40 kJ/kg. We show that it is critical to weld the interfaces between nanofibers and introduce intrinsically high-energy phases (nanocrystalline domains) into nanofibers.

INTRODUCTION

Nanofibrous hydrogels are pervasive in the bodies of animals[1] and plants.[2] Owing to the merits of high porosity, high water content, and biocompatibility,[3–6] nanofibrous hydrogels have been explored in diverse applications, including tissue regeneration,[7–9] ionic skin,[10] hemostatic dressings,[11] cartilage repair,[12] imperceptible textile sensors,[13,14] printable electrodes for flexible implants,[15] tissue adhesives,[16,17] and small-scale bio-robots.[18] Electrospinning represents one of the most widely used methods for fabricating nanofibrous hydrogels, since electrospinning gives relatively uniform fiber diameters and tunable fibrous architectures.[3] Existing electrospun nanofibrous hydrogels[19–22] are typically weak and fragile because of the low strength of nanofibers and the weak interface between nanofibers. In particular, when an electrospun nanofibrous hydrogel is hydrated, the presence of water gradually swells the nanofibers and attacks the interface between nanofibers, leading to a weak and brittle nanofibrous network. Efforts have been made by introducing strong chemical crosslinks to enhance the strength and toughness of nanofibrous hydrogels under a single cycle of mechanical load.[23,24] However, such reinforced nanofibrous hydrogels are still susceptible to fatigue failures under multiple cycles of mechanical loads.[25]

A bouligand structure is common for mineralized natural materials and has been widely reproduced in synthetic hard materials.[26] However, engineering bouligand structure in soft hydrogels has been challenging. A recent study reports that the

Progress and potential

Nanofibrous hydrogels are pervasive in animal and plant bodies. Most biological nanofibrous hydrogels can maintain their high strength and high toughness under cyclic loads by optimizing their hierarchical assembly. However, such superior mechanical properties are rarely achieved in synthetic nanofibrous hydrogels. Here, we explore the possibility of engineering a bouligand-type, welded, and high-crystalline fibril structure in synthetic hydrogels, which gives highly enhanced strength and toughness over long-term dynamic loading. The resultant nanofibrous hydrogel also shows superior impact resistance, further suggesting its potential as the next-generation flexible protective fabric.

soft membrane in the lobster underbelly is also composed of the bouligand multilayered structure, which imparts the natural hydrogel with an extremely high fracture toughness (i.e., 24.98 MJ/m^3) and tensile strength (i.e., 23.36 MPa) under cyclic loading.[27] Here, we report a bioinspired design of strong and fatigue-resistant nanofibrous hydrogels that can closely mimic the bouligand structure of soft membranes in lobster underbelly (Figure 1). The bouligand-type nanofibrous hydrogel achieves a high nominal strength up to 8.4 MPa and fatigue threshold up to 770 J/m^2 for electrospun nanofibrous hydrogels. In addition, it can bear 3,000 times its weight at the dry state after prolonged cyclic loading under the tensile stress of 1 MPa, and possess the superior specific penetration energy of 40 $\pm$ 5 kJ/kg at the hydrated state for superior impact resistance, comparable with that of polyethylene. We propose that it is critical to weld the interfaces between nanofibers and introduce intrinsically high-energy phases (i.e., nanocrystalline domains) in nanofibers (Figure 2). To validate this hypothesis, we chose polyvinyl alcohol (PVA) as a model material system of nanofibrous hydrogels with tunable crystallinities in nanofibers and adjustable interfaces between nanofibers. We show that the PVA nanofibrous hydrogels with both high-crystalline nanofibers and welded interfaces between nanofibers can reach a high strength of 3.5 MPa and high fatigue threshold of 600 J/m^2, comparable with the corresponding properties of biological nanofibrous hydrogels.[28] Our simulations of the nanofibrous network further quantify the contribution of interfacial strength between nanofibers to the overall strength of the nanofibrous network. In addition, we develop a theoretical model that accounts for the relationship between the nanofibrous structures and the fatigue threshold of the fibrous networks. This work suggests the potential of our nanofibrous hydrogels as flexible hydrogel-based protective fabrics and textile electronics.

RESULTS

Design and fabrication of nanofibrous hydrogels

Our method to fabricate the strong and fatigue-resistant nanofibrous PVA hydrogels is based on a unique approach involving the sequential processes of electrospinning, welding, and dry annealing (Figure S1). We first use high voltage (i.e., 10 kV) to eject charged threads of PVA polymer solution to form a nanofibrous PVA film on a flat collector.[29] Upon collection, the electrospun nanofibrous PVA film usually gives weak interfaces between neighboring nanofibers; consequently, the neighboring layers of nanofibers can even form gaps in between, as manifested by the scanning electron microscopy (SEM) images in Figure 3A. In addition, each nanofiber has a relatively low crystallinity of 11.4 wt% in the dry state (Figure 3F), measured by differential scanning calorimetry (DSC) (Figure 3H). We take the electrospun nanofibrous PVA film upon collection as a control sample of the nanofibrous hydrogel with low crystallinity and weak interface (Figure 3A).

After the electrospinning process, we weld the interfaces between nanofibers through a process of water vapor exposure.[3] Specifically, the electrospun nanofibrous PVA film is transferred into a humidity chamber and exposed to water vapor. The water vapor gradually dissolves the outermost surfaces of the PVA nanofibers, and a welded interface forms between adjacent nanofibers (Figure 3C).[3] The slight increase of the fiber diameter from 750 nm to 1.1 μm manifests the welding-assisted deformation of the PVA nanofibers (Figures 3E and S2). While the strength of the welded nanofibrous network increases with the water vapor exposure time, overexposure of water vapor can fully dissolve the PVA nanofibers, giving an impaired nanofibrous structure.[3] Therefore, we set a moderate water vapor exposure time of 6 min to ensure strong interfaces between nanofibers while preserving the

[1]Department of Mechanical Engineering, Massachusetts Institute of Technology, Cambridge, MA 02139, USA

[2]Department of Civil and Environmental Engineering, Syracuse University, Syracuse, NY 13244, USA

[3]Institute for Soldier Nanotechnologies, Massachusetts Institute of Technology, Cambridge, MA 02139, USA

[4]Department of Chemistry, Massachusetts Institute of Technology, Cambridge, MA 02139, USA

[5]Hansen Experimental Physics Laboratory, Stanford University, Stanford, CA 94305

[6]U.S. Army Combat Capabilities Development Command, Army Research Laboratory, RDRL-WMM-G, Aberdeen Proving Ground, MD 21005-5069, USA

[7]Department of Aeronautics and Astronautics, Massachusetts Institute of Technology, Cambridge, MA 02139, USA

[8]Department of Civil and Environmental Engineering, Massachusetts Institute of Technology, Cambridge, MA 02139, USA

[9]These authors contributed equally

[10]Lead contact

*Correspondence: zhaox@mit.edu

https://doi.org/10.1016/j.matt.2021.03.023

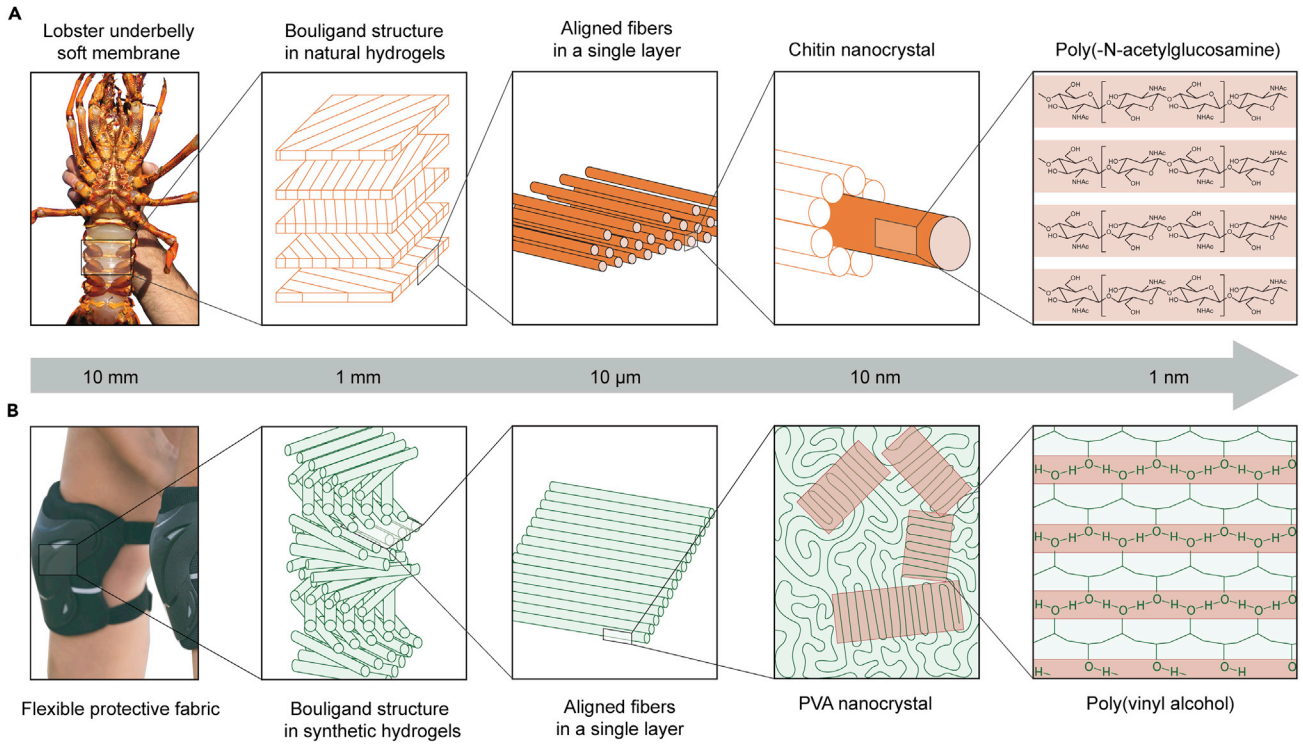

Figure 1. Bioinspired design of strong and fatigue-resistant nanofibrous hydrogels

(A) The natural hydrogel membrane in a lobster underbelly is composed of the bouligand-type multi-layered structure with a 36° rotation between the adjacent layers of aligned chitin fibers. The chitin fibers contain alternating amorphous and nanocrystalline chitin, which are long-chain poly-*N*-acetylglucosamine at the molecular level.

(B) We designed synthetic nanofibrous hydrogels that closely reproduce the bouligand structure of the natural hydrogel membrane in a lobster underbelly, and can be potentially used as flexible protective fabrics materials. A single layer in the bouligand structure consists of aligned fibers, and each fiber contains amorphous and nanocrystalline PVA.

nanofibrous PVA structure. To introduce substantial nanocrystalline domains in nanofibers, we further dry the welded PVA nanofibrous film in an incubator at 50°C for 0.5 h, followed by annealing at 100°C for 1 h. The crystallinity of the dry-annealed sample substantially increases up to 41 wt% in the dry state (Figures 3F and 3H). The average size of the nanocrystalline domains in the dry-annealed sample is measured to be 3.7 nm (Figures 3G and 3I), greater than that of the sample upon collection (i.e., 1.8 nm, Figures 3G and 3I), indicating the growth of nanocrystalline domains upon dry annealing. The resultant PVA nanofibrous film with combined welding, drying, and annealing forms the nanofibrous hydrogel with high crystallinity and strong interface (Figure 3D).

We further fabricate the other two control samples for comparison and analysis. We anneal the electrospun nanofibrous PVA film upon collection at 100°C for 1 h, representing the nanofibrous hydrogel with high crystallinity and weak interface (Figure 3B). In addition, we transfer the electrospun nanofibrous PVA film upon collection into a humidity chamber and expose it to the glutaraldehyde vapor, which crosslinks the polymer chains in the nanofibers and at the interfaces of neighboring nanofibers.[27] The resultant nanofibrous hydrogel possesses welded interfaces between nanofibers from the SEM image (Figure 3C) but contains negligible crystallinity enhancement based on the DSC measurement (Figure 3F), thereby representing the nanofibrous hydrogel with low crystallinity and strong interface (Figure 3C).

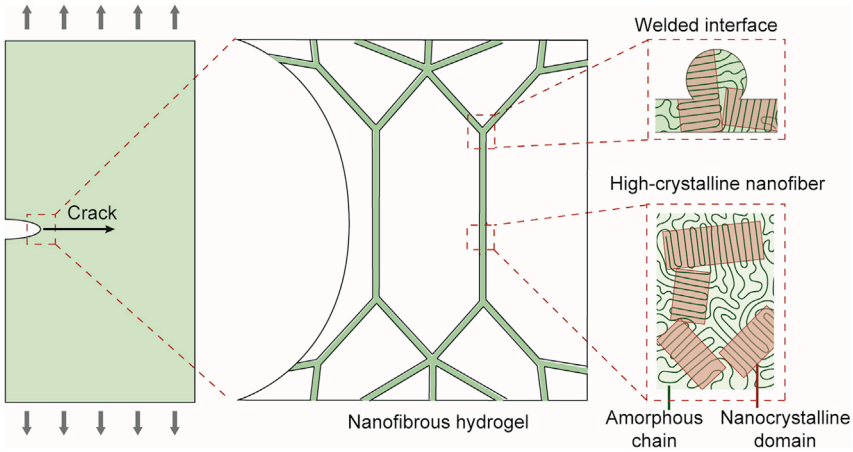

Figure 2. The principle for the design of strong and fatigue-resistant nanofibrous hydrogels
The strong and fatigue-resistant nanofibrous hydrogels require the synergy of a strong welded interface between nanofibers and high-crystalline nanofibers to resist propagation of fatigue crack.

Mechanical characterization of nanofibrous hydrogels

We first characterize the mechanical properties of various nanofibrous hydrogels in hydrated state under a single cycle of uniaxial tension. As shown in Figure 3J, the nanofibrous hydrogel with low crystallinity and weak interface fails to bear any mechanical load when the sample is immersed in water since it dissociates into isolated nanofibers. In comparison, the nanofibrous hydrogel with low crystallinity and strong interface shows a high strength of 4 MPa, but suffers from brittle fracture with an ultimate stretch of only 1.2 due to the highly crosslinked polymers by glutaraldehyde. The stretchability of the nanofibrous hydrogel with high crystallinity and weak interface can reach 2.25, but its strength is only 1.4 MPa. In contrast, the nanofibrous hydrogel with high crystallinity and strong interface demonstrates both high strength (3.5 MPa) and high stretchability (3.4). The difference between the highly crystalline nanofibrous hydrogels with the welded (strong) interface and the unwelded (weak) interface is analogous to the difference between bacterial cellulose nanofibrous hydrogels and nanocellulose hydrogels. Both bacterial cellulose nanofibrous hydrogels and nanocellulose hydrogels contain nanocrystalline domains. Bacterial cellulose nanofibrous hydrogels contain strong crosslinks (strong interface) between fibers, while nanocellulose hydrogels have negligible crosslinks (weak interface).[30–32] The strong interface between fibers in bacterial cellulose nanofibrous hydrogels gives their high tensile strength,[30,31] while the weak interface between fibers in nanocellulose hydrogels renders their low tensile strength.[32]

We further characterize the fatigue properties of various nanofibrous hydrogels under dynamic cyclic loading. The fatigue thresholds are measured following the single-notch method (see details in the experimental procedures).[25,33] As shown in Figure 3K, the fatigue threshold of the nanofibrous hydrogel with high crystallinity and strong interface reaches 600 J/m^2, which is significantly enhanced compared with the control samples (i.e., 41 J/m^2 for the nanofibrous hydrogel with low crystallinity and strong interface, and 320 J/m^2 for the nanofibrous hydrogel with high crystallinity and weak interface shown in Figure 3M and S3). To further evaluate the resistance to fatigue crack propagation, we use the Paris law to fit the measured curve of the fatigue crack extension rate

$$dc / dN = AG^m, \qquad \text{(Equation 1)}$$

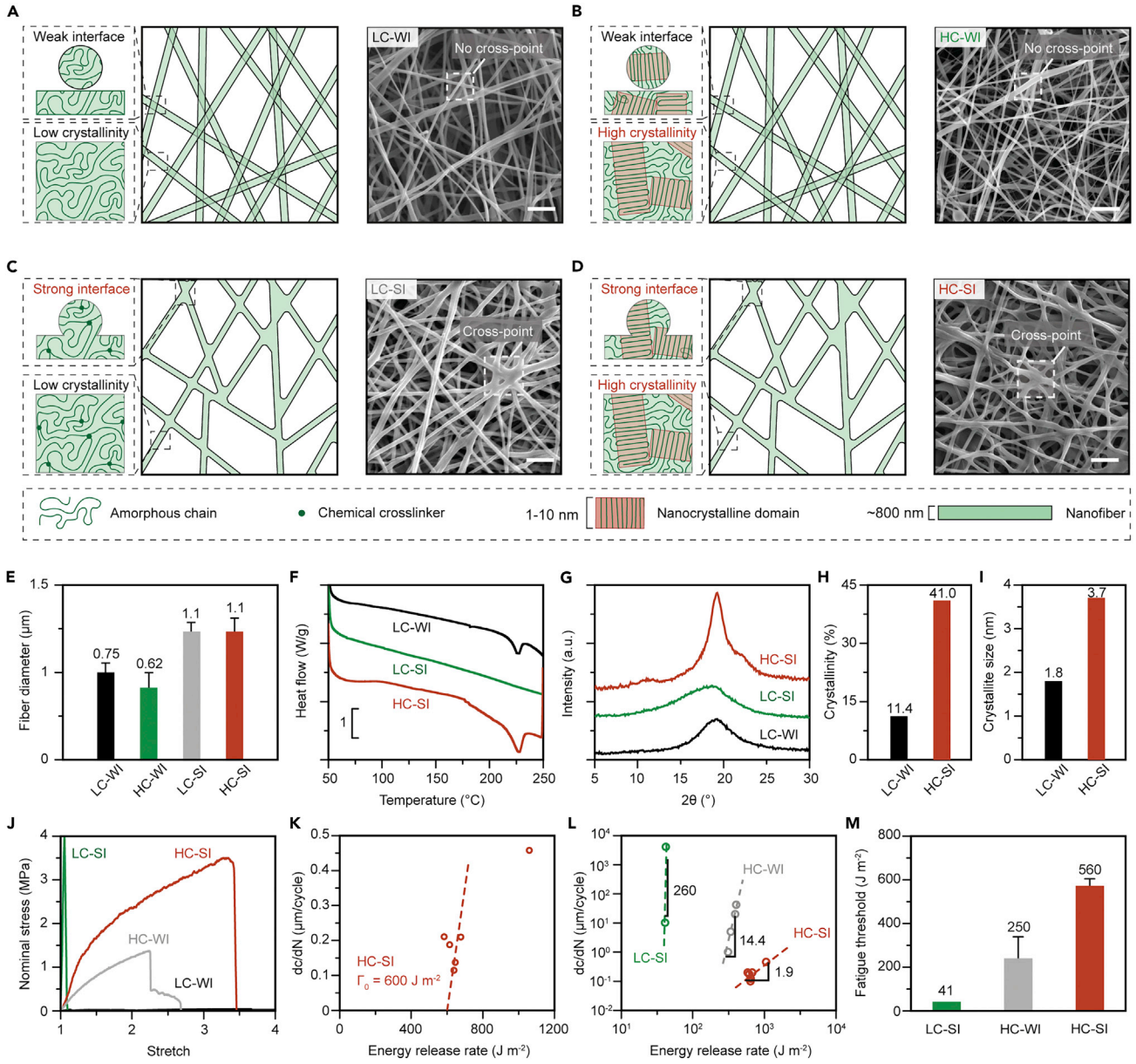

Figure 3. Structural and mechanical characterizations of nanofibrous hydrogels

(A–D) Structural characterizations of nanofibrous hydrogels. Schematics and SEM images of (A) the nanofibrous hydrogel with low crystallinity and weak interface (i.e., LC-WI), (B) the nanofibrous hydrogel with high crystallinity and weak interface (i.e., HC-WI), (C) the nanofibrous hydrogel with low crystallinity and strong interface (i.e., LC-SI), and (D) the nanofibrous hydrogel with high crystallinity and strong interface (i.e., HC-SI).

(E) The average fiber diameters for various nanofibrous hydrogels, including LC-WI, HC-WI, LC-SI, and HC-SI hydrogels.

(F) DSC curves for the nanofibrous hydrogels, including LC-WI, LC-SI, and HC-SI hydrogels.

(G) Wide-angle X-ray scattering curves for the nanofibrous hydrogels, including LC-WI, LC-SI, and HC-SI hydrogels.

(H and I) (H) Crystallinity at the dry state and (I) average size of crystalline domains of the nanofibrous hydrogels, including LC-WI and HC-SI hydrogels.

(J) Nominal stress versus stretch curves under a monotonic tensile loading for various nanofibrous hydrogels, including LC-WI, HC-WI, LC-SI, and HC-SI hydrogels.

(K) Crack extension rate versus applied energy release rate for the nanofibrous hydrogel with high crystallinity and strong interface (HC-SI), from which the fatigue threshold is identified as 600 J/m^2.

(L) Log-log plot of crack extension rate versus applied energy release rate of various nanofibrous hydrogels, including LC-SI, HC-WI, and HC-SI hydrogels.

(M) Fatigue thresholds of various nanofibrous hydrogels, including LC-SI, HC-WI, and HC-SI hydrogels. The number value above the column represents the mean value of measured fatigue thresholds. Scale bars, 10 μm in (A–D). Data in (E) and (M) are represented as mean ± SEM.

where dc/dN is the crack extension per cycle and G is the applied energy release rate, and A and m are material constants.[34] The Paris law exponent m denotes the resistance to fatigue crack propagation, which can be identified from the slope of the crack extension rate versus energy release rate on the log-log scale. As shown in Figure 3L, the values of m for the nanofibrous hydrogel with low crystallinity and strong interface and the nanofibrous hydrogel with high crystallinity and weak interface are 260 and 14.4, respectively, indicating that they are prone to fast fatigue crack propagation. In contrast, the value of m for the nanofibrous hydrogel with high crystallinity and strong interface is 1.9, slightly lower than that of common elastomers (e.g., ~2–3 for natural rubber and styrene-butadiene rubber),[35] indicating its high resistance to crack propagation under cyclic loading.

Simulation of deformation of nanofibrous networks

We further develop a nanofibrous network model to simulate the mechanical response of nanofibrous networks under tensile loading (see the supplemental information). The nominal stress versus nominal strain curve of a single fiber (i.e., σ_{fiber} versus ε) in the network under tension is modeled by a tri-section potential with its spring constants fitted from the experimental results (Figure S4), and the nominal tensile strength of the fiber is denoted as $S_{\text{fiber}}^{\text{strength}}$. The interface between fibers in contact is modeled by a truss element with the same cross-section area as the fiber. The nominal stress versus nominal strain relation of the interfacial truss element (i.e., $\sigma_{\text{interface}}$ versus ε) can be expressed as

$$\sigma_{\text{interface}} = C_1 \sigma_{\text{fiber}}(\varepsilon / C_2), \qquad \text{(Equation 2a)}$$

and the nominal tensile strength of the interfacial truss is expressed as

$$S_{\text{interface}}^{\text{strength}} = C_1 S_{\text{fiber}}^{\text{strength}}, \qquad \text{(Equation 2b)}$$

where C_1 and C_2 are two non-dimensional parameters. When $C_1 = C_2 = 1$, the fiber and the interfacial truss have the same nominal stress versus nominal strain relation and the same nominal tensile strength.

In a set of simulations of the network under tension, we keep the network topology and the σ_{fiber} versus ε relation constant, while systemically changing the interfacial interaction between nanofibers in contact by varying C_1 and C_2. Figures 4A and 4B show the snapshots from the simulations of fibrous networks with strong interface (i.e., $C_1 = 1$, $C_2 = 1$) and weak interface (i.e., $C_1 = 0.05$, $C_2 = 1$) under tension. The fibrous network with strong interface can maintain the integrity of connected fibers at large deformation (i.e., $\lambda = 3.3$), while the fibrous network with weak interface disintegrates at relatively small deformation (i.e., $\lambda = 1.8$). We further systematically adjust the interfacial strength by keeping $C_2 = 1$ while setting C_1 as 1, 0.5, 0.25, 0.1, 0.05, 0.025 (Figure 4C). As shown in Figure 4D, the fibrous network becomes weaker and less stretchable as the interfacial strength decreases. We further adjust the stretchability of the interface by keeping $C_1 = 1$ while setting C_2 as 1, 0.5, 0.25, 0.1 (Figure 4E). The nominal stress versus stretch curves of the corresponding fibrous networks are nearly identical with each other (Figure 4F). Our simulation results suggest that the mechanical response of the fibrous network is mainly governed by the strength instead of the extensiblity of the interface.

Theory for fatigue threshold of nanofibrous networks

The fatigue crack propagation in nanofibrous networks is analogous to that in polymer networks, which has been explained by the Lake-Thomas model.[36] The fatigue threshold of a nanofibrous network is mainly attributed to the fracture energy of a single layer of nanofibers at the crack path (Figure 5A). As shown in the *in situ*

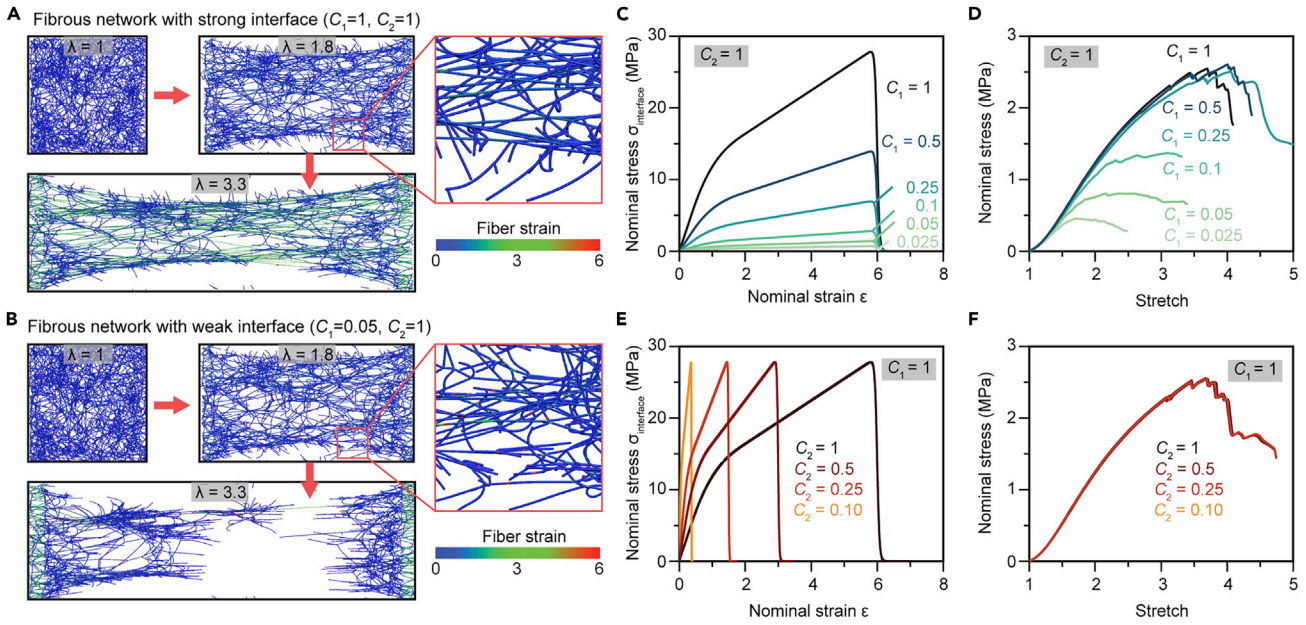

Figure 4. Simulation of nanofibrous networks under tensile loading

(A) Snapshots of the nanofibrous network with strong interface (i.e., C_1 = 1, C_2 = 1) at various stretches of 1, 1.8, and 3.3.

(B) Snapshots of the nanofibrous network with weak interface (i.e., C_1 = 0.05, C_2 = 1) at various stretches of 1, 1.8, and 3.3. The colors in (A) and (B) represent the fiber strain distribution in the nanofibrous networks.

(C) Nominal stress versus nominal strain curves of the interface with the same ultimate strain (C_2 = 1) but different strengths (C_1 = 0.025–1).

(D) Nominal stress versus stretch curves of the fibrous networks constructed by the interface with the same ultimate strain (C_2 = 1) but different strengths (C_1 = 0.025–1).

(E) Nominal stress versus nominal strain curves of the interface with the same strength (C_1 = 1) but different ultimate strains (C_2 = 0.1–1).

(F) Nominal stress versus stretch curves of the fibrous networks constructed by the interface with the same strength (C_1 = 1) but different ultimate strains (C_2 = 0.1–1).

confocal laser scanning microscopy images in Figure 5C and 5D and the SEM images in Figure S5, the pre-existing crack shows a significant blunting and propagates by the scission of the aligned bridging nanofibers on the crack path. Based on this observation, we propose the following model for the fatigue thresholds of nanofibrous networks (or fibrous networks in general),

$$\Gamma_0 = \alpha n_{fiber} U_{fiber} L_{fiber}, \qquad \text{(Equation 3)}$$

where α>1 is a non-dimensional parameter, n_{fiber} is the number of active nanofibers (i.e., the nanofibers that can bear mechanical loads) per unit volume of the nanofibrous network in the swollen state, U_{fiber} is the energy required to fracture a single nanofiber after prolonged cyclic loading, and L_{fiber} is the average length of the nanofibers between adjacent crosslinkers in the nanofibrous network in the undeformed state.

Assuming that there are negligible inactive nanofibers in the nanofibrous network, the number density of the active nanofibers in the swollen state n_{fiber} and the volume fraction of the nanofibers in the film in the swollen state Φ have the following relation:

$$\Phi = \frac{\pi n_{fiber} D_{fiber}^2 L_{fiber}}{4}. \qquad \text{(Equation 4)}$$

Therefore, based on Equation 4, the n_{fiber} value can be determined by the measured values of Φ, D_{fiber}, and L_{fiber}. The energy required to fracture a single nanofiber after prolonged cyclic loading U_{fiber} can be experimentally identified using the following equation

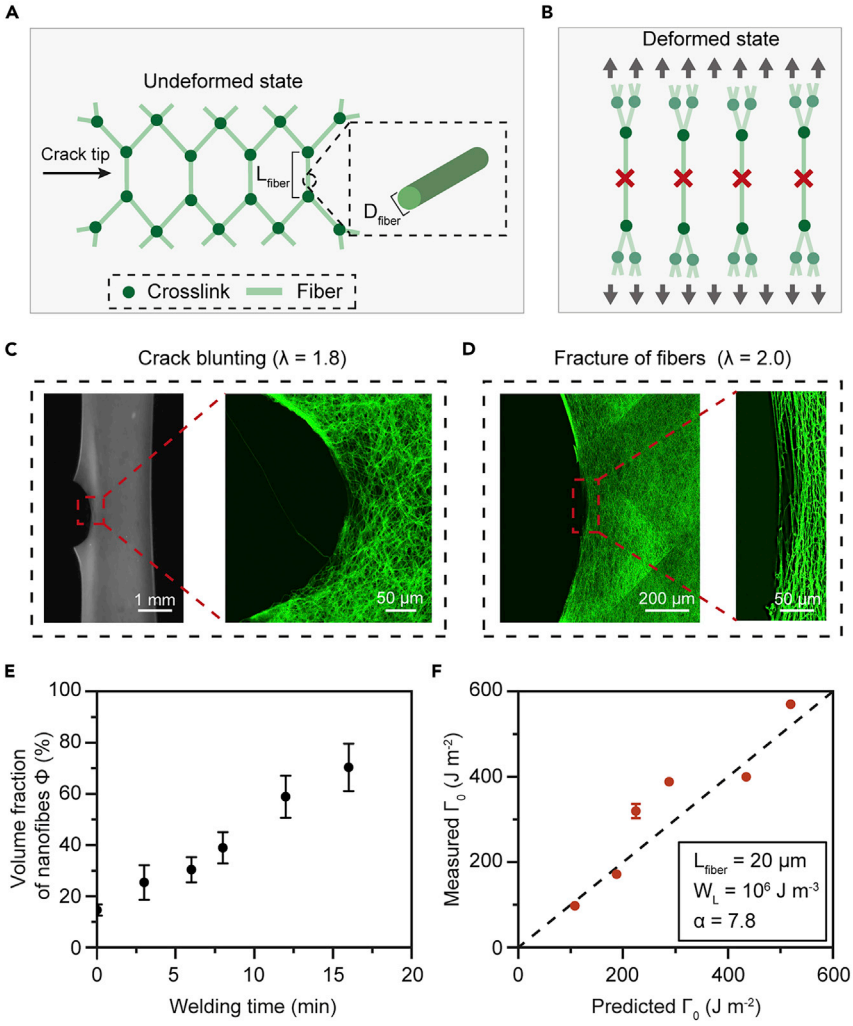

Figure 5. Theoretical model for predicting the fatigue threshold of nanofibrous hydrogel networks

(A) Schematic of the bridging nanofibers at the crack path at the undeformed state.

(B) Schematic of the bridging nanofibers at the crack path at the highly deformed state before fracture. The red cross indicates the scission of the nanofibers on the crack path when the crack extends.

(C) Bright-field and confocal images of a notched nanofibrous hydrogel sample with a blunt crack tip before crack initiation at the applied stretch of 1.8 (λ = 1.8).

(D) Confocal images of a notched nanofibrous hydrogel sample with nanofibers fractured at the crack tip during crack propagation at the applied stretch of 2.0 (λ = 2.0).

(E) Volume fraction of nanofibers in various nanofibrous hydrogels tuned by the welding time of the hydrogels.

(F) Comparison between experimentally measured fatigue thresholds with the theoretically predicted fatigue thresholds of various nanofibrous hydrogels ($\alpha = 7.8$, $W_L = 10^6$ J/m^3, $L_{fiber} = 20$ μm). Scale bars, 1 mm and 50 μm in (C) and 200 and 50 μm in (D), from left to right. Data in (E) and (F) are represented as mean ± SEM.

$$U_{fiber} = \frac{\pi W_L D_{fiber}^2 L_{fiber}}{4}, \qquad \text{(Equation 5)}$$

where W_L is the maximum strain energy density that a nanofiber can sustain without fatigue failure under cyclic tensile loads. By substituting Equations 4 and 5 into Equation 3, we can get the expression for the fatigue threshold of the nanofibrous network as

$$\Gamma_0 = \alpha \Phi W_L L_{fiber}. \quad \text{(Equation 6)}$$

To validate Equation 6, we fabricate a series of nanofibrous hydrogels with varying values of Φ while maintaining W_L and L_{fiber} approximately constant. We keep the same fabrication conditions for the processes of electrospinning and dry annealing, so that the parameters $W_L$and L_{fiber}can be fixed for the series of nanofibrous hydrogels. The average length of the nanofibers in the nanofibrous hydrogel L_{fiber} is measured to be around 20 μm from the SEM image in Figures 3D and S2. The maximum strain energy density W_L is identified to be 4.8×10^6 J/m^3 by the fatigue test of a single nanofiber (the detailed experimental procedure is provided in the supplemental information and Figures S6–S9). In addition, by varying the welding time from 0 to 16 min, the nanofiber volume fraction Φ can be readily tuned from 14.6% to 70.3% (Figure 5C). As the welding time increases, the sample gets thinner, thereby increasing the nanofiber volume fraction.

As shown in Figure 5D, our model gives a quantitative prediction for the experimental results with the parameter $\alpha = 7.8$, which is higher than the value for the intrinsic fracture energy of polymer networks (~3).[37] This indicates that, in addition to the energy required to fracture a layer of bridging nanofibers on the crack path, other effects can also contribute to the fatigue thresholds of the nanofibrous hydrogels. For example, the nanofibrous network can contain topological defects, which lead to effectively longer bridging nanofibers for the enhanced fatigue threshold. Moreover, the nanofibers after prolonged cyclic loading typically show a stiffening stress-strain relation, which could lead to highly stretched nanofibers around the crack tip, retarding the crack propagation.

Bouligand-type nanofibrous hydrogel as lobster underbelly-inspired protective fabric

The soft membrane in the underbelly of the American lobster is a hydrogel that contains 90 wt% water and exhibits extremely high fracture toughness (i.e., 24.98 MJ/m^3) and tensile strength (i.e., 23.36 MPa) under cyclic loading.[27] Recent studies further revealed that the extraordinary mechanical properties of the lobster underbelly are mainly attributed to its unique multi-layered nanofibrous structure which consists of aligned chitin nanofibers in each layer.[27] The neighboring two layers of aligned chitin fibers have a 36° twisting angle. The chitin fiber consists of long-chain polymers of poly-*N*-acetylglucosamine (Figure 1A), which are assembled into semi-crystalline structures with alternating amorphous and nanocrystalline domains. Here, we demonstrate a lobster underbelly-inspired nanofibrous hydrogel for potential application as a flexible protective fabric. We first fabricate a single layer of aligned nanofibrous PVA film by ejecting charged threads of PVA polymer solution on a rotating cylinder collector. Five layers of aligned nanofibrous PVA films are further stacked together with a twisting angle of approximately 36° between the adjacent films (Figures 6A and 6B), mimicking the layered nanofibrous structure of the soft membrane in the lobster's underbelly.[27] The stacked films are further transferred into a humid chamber for subsequent dissolving-assisted welding process to form the strong interfaces between adjacent layers. As schematically illustrated in Figure 1B, the resultant nanofibrous hydrogel shows a bouligand-type structure with rotating layers, each of which is composed of aligned nanofibers. Such bouligand-type structure is verified by the SEM images (Figures 6A and 6B).

We first characterize the mechanical properties of the bouligand-type nanofibrous hydrogel under a single cycle of load. The nominal tensile strength of the bouligand-type nanofibrous hydrogel can reach as high as 8.4 and 7.4 MPa in the

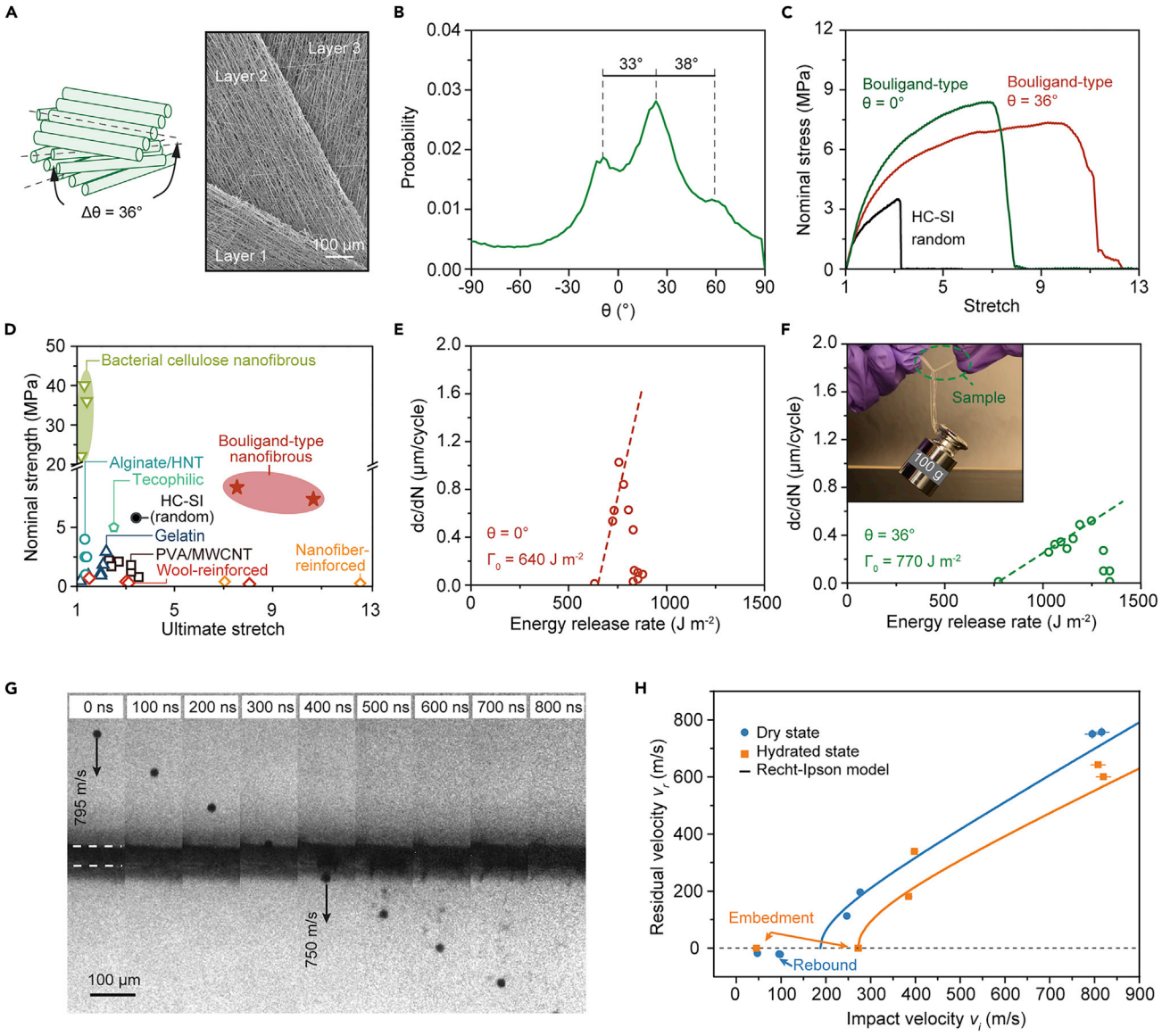

Figure 6. Design and characterization of the bouligand-type nanofibrous hydrogel

(A) Schematic of the bouligand-type nanofibrous hydrogel and the corresponding SEM image.

(B) Probability histogram of the rotating angles of nanofibers on each layer.

(C) Nominal stress versus stretch curves of the bouligand-type nanofibrous hydrogel with the loading direction of $\theta = 0°$ and $\theta = 36°$, and the randomly distributed nanofibrous hydrogel with high crystallinity and strong interface (i.e., HC-SI).

(D) Comparison chart of various reported nanofibrous hydrogels, the randomly distributed nanofibrous hydrogel with high crystallinity and strong interface (i.e., HC-SI), and the bouligand-type nanofibrous hydrogel, in terms of nominal strength and ultimate stretch.

(E) Crack extension rate versus applied energy release rate for the bouligand-type nanofibrous hydrogel with the loading direction of $\theta = 0°$.

(F) Crack extension rate versus applied energy release rate for the bouligand-type nanofibrous hydrogel with the loading direction of $\theta = 36°$. Inset: the bouligand-type nanofibrous hydrogel bears 3,000 times its own weight at the dry state after dynamic loading (i.e., tensile stress of 1 MPa for 5,000 cycles).

(G) Multi-frame sequence of a high-velocity impact loading on the bouligand-type nanofibrous hydrogel in the dry state by a steel microparticle at 795 m/s.

(H) Comparison of the residual velocity as a function of the impact velocity for the bouligand-type nanofibrous hydrogel in the dry and hydrated states. A positive residual velocity indicates perforation, a negative velocity indicates rebound, and a zero velocity indicates embedment.

Scale bars, 100 μm in (A) and (G).

directions of $\theta = 0^\circ$ and $\theta = 36^\circ$, respectively (θ is defined as the angle between the applied load and the direction of aligned nanofibers at the bottom layer). The ultimate stretch of the bouligand-type nanofibrous hydrogel can reach as high as 7.4 and 10.7 in the directions of $\theta = 0^\circ$ and $\theta = 36^\circ$, respectively (Figure 6C). Compared with the nanofibrous hydrogels with randomly oriented nanofibers (Figure 3J), the bouligand-type nanofibrous hydrogel demonstrates substantial enhancements in both the tensile strength and stretchability. We summarize the nominal tensile strength and ultimate stretch of various nanofibrous hydrogels reported in literature[38–45] in Figure 6D. The tensile strengths of existing nanofibrous hydrogels, including PVA and PVA blended with chitosan,[38] crosslinked and uncrosslinked gelatin,[39–42] alginate filled with halloysite nanotubes,[43] and sodium polyacrylate blended with tecophilic polymers,[44] are typically lower than 4 MPa, and their ultimate stretches are below 3. Tough hydrogels reinforced by wools[45] or nanofibers[46] can be stretched up to 10 times their original lengths, but they suffer from low tensile strength (around 0.2 MPa). Bacterial cellulose nanofibrous hydrogels can achieve a high tensile strength of 20–40 MPa, but these hydrogels have ultimate stretches below 1.5 since the introduced bacterial cellulose themselves have relatively low fracture strains.[30,31] Notably, the bouligand-type nanofibrous hydrogel outperforms existing nanofibrous hydrogels in both tensile strength and ultimate stretch. However, the bouligand-type nanofibrous hydrogel's tensile strength is still inferior to that of the lobster underbelly. The microstructure of the lobster underbelly is much more complex and hierarchical.[47] In the lobster underbelly, the chitin macromolecules are arranged in an antiparallel fashion forming alpha-chitin chains, 18–25 of which form nanofibers with diameters of 2–5 nm and lengths around 300 nm. The nanofibers further form fibers with diameters of 50–350 nm, assembling to form a bouligand-type structure. The bouligand-type nanofibrous hydrogel in this work can only mimic part of the structural features of the lobster underbelly.

We further characterize the fatigue performances of the bouligand-type nanofibrous hydrogel. As shown in Figures 6E and 6F, the fatigue threshold in the directions of $\theta = 0^\circ$ and $\theta = 36^\circ$ can reach up to 640 and 770 J/m^2, respectively, comparable with the fatigue thresholds of nanofibrous biological tissues.[33] To further verify the superior fatigue-resistant properties of the bouligand-type nanofibrous hydrogel, we deform the sample to the stress level of 1 MPa for 5,000 cycles and show that it can still bear 3,000 times its own dry weight under tension (Figure 6F, inset).

We further conduct high-velocity microparticle impact experiments to characterize the impact resistance of the bouligand-type nanofibrous hydrogel. In these experiments, we impact the sample in both the dry and hydrated states with 17 $\pm$ 1 μm diameter steel particles over a range of impact velocities V_i up to 800 m/s. For high-velocity impacts (Figure 6G), the steel microparticle perforates the film and exits at a reduced residual velocity V_r. The ratio of V_r over V_i defines the coefficient of restitution. Figure 6H plots the residual velocity V_r as a function of impact velocity V_i for the bouligand-type nanofibrous hydrogel in both dry state and hydrated state. We further obtain the specific energy of penetration of the bouligand-type nanofibrous hydrogel by calculating the ratio of the kinetic energy loss over the mass of the sample (see details in the experimental procedures). The specific energy of penetration remaining is 70 $\pm$ 10 kJ/kg for the sample in the dry state and 40 $\pm$ 5 kJ/kg for the sample in the hydrated state, which is comparable with that of polyethylene.[48] The above results demonstrate the potential applications of the bouligand-type nanofibrous hydrogel as flexible, lightweight, and impact-resistant protective fabrics and textile electronics.

DISCUSSION

Existing hydrogels are mostly homogeneous, lacking structural heterogeneity, and are unable to match the mechanical properties of biological tissues. In this work, we provide a general strategy to design fatigue-resistant nanofibrous hydrogels by engineering nanofibers and nanocrystalline domains across varying length scales. We show that the synergy of introducing nanocrystalline domains into nanofibers and welding of neighboring nanofibers can remarkably enhance the fatigue threshold of nanofibrous hydrogels from 41 to 600 J/m^2. Inspired by the nanofibrous structure found in the lobster underbelly, we also demonstrate a bouligand-type nanofibrous hydrogel with further enhanced nominal strength up to 8.4 MPa, fatigue threshold up to 770 J/m^2, and specific penetration energy of impact resistance up to 70 $\pm$ 10 kJ/kg in the dry state and 40 $\pm$ 5 kJ/kg in the hydrated state. This work suggests an avenue toward the next generation of nanofibrous hydrogels for diverse emerging applications, including artificial replacement, lightweight physical protection, textile electronics, smart clothing, and tissue engineering scaffolds.

EXPERIMENTAL PROCEDURES

Resource availability

Lead contact

Further information and requests for resources and materials should be directed to and will be fulfilled by the lead contact, Xuanhe Zhao (zhaox@mit.edu).

Materials availability

All unique/stable reagents generated in this study are available from the lead contact without restriction.

Data and code availability

The published article includes all data generated or analyzed during this study.

Fabrication of fatigue-resistant nanofibrous hydrogels

The aqueous solution for electrospinning contains 10 wt% PVA (MW 146,000–186,000, 99+% hydrolyzed; MilliporeSigma) and 0.5 vol% Triton X-100 (MilliporeSigma) as a surfactant. The aqueous PVA solution was ejected by a syringe pump (New Era Pump Systems, Inc.) with a flow rate of 0.01 mL/min at ambient temperature and relative humidity of 25%. A high voltage (10 kV) was applied between the syringe pump and a grounded aluminum foil on a flat plate or a rotating drum. The charged thread of PVA solution was collected by the aluminum foil for 3 h, resulting in a PVA film with randomly distributed nanofibers on the flat plate, or a PVA film with aligned nanofibers on the rotating drum collector (1,000 rpm). After electrospinning, the PVA film was transferred into a closed chamber for welding at high humidity (>90% relative humidity). The chamber containing deionized water was placed on a hot plate with controlled temperature of 60°C to create the high-humidity environment. We control the time for welding from 0 to 16 min to tune the porosity and polymer content of the resultant nanofibrous PVA film. The PVA film after welding was then dried in an incubator at low humidity (<20% relative humidity) and 30°C for 30 min to remove residual water, followed by annealing at 100°C for 1 h to introduce the nanocrystalline domains in the nanofibers. Thereafter, the PVA film was swollen in water, resulting in a nanofibrous hydrogel with either randomly distributed nanofibers or aligned nanofibers.

Fabrication of bouligand-type nanofibrous hydrogels

Upon electrospinning, five layers of aligned nanofibrous PVA films were assembled into a helicoidal architecture in which each layer rotates by 36° relative to the

adjacent one. The bouligand-type assembly was then welded in a closed chamber with high humidity (>90% relative humidity) to introduce strong interfaces between the adjacent layers. The resultant multi-layered bouligand-type nanofibrous PVA film was further dried at 50°C for 30 min and annealed at 100°C for 1 h. Thereafter, the PVA film was swollen in water, resulting in a bouligand-type nanofibrous hydrogel.

Simulation of coarse-grained nanofibrous network

The nanofibrous network was constructed by the assembly of 673 nanofibers, and each of them was explicitly modeled by a coarse-grained bead-spring model. The coarse-grained model had been developed to study the mechanics of the cytoskeleton and fibrous membrane materials,[27,49] and used to compare the failure mechanism of the nanofibrous network by adjusting the topology, fiber length, as well as the nonlinear mechanical properties of nanofibers and the interfaces between adjacent nanofibers. The simulations were performed by using a LAMMPS package.[50] The initial model and modification of the fiber interactions at the interfaces were generated by using our MATLAB scripts (see the supplemental information).

Fatigue characterization

Fatigue tests were performed using a UStretch testing machine (CellScale) at a strain rate of 5 mm/s. The samples were submerged in a water bath to prevent dehydration.[25,33] We adopted the single-notch method to measure the fatigue threshold. We first applied a cyclic loading of a maximum stretch λ_a on a notched sample with a pre-existing crack length smaller than one-fifth of its width. A digital microscope (AM4815ZT, Dino-Lite; resolution, 20 mm/pixel) was used to record the crack initiation and crack extension over cycles $c(N)$. The applied energy release rate can be calculated by $G(\lambda_a, N) = 2k(\lambda_a)c(N)W(\lambda_a, N)$, where $k = 3/\sqrt{\lambda_a}$, c is the crack length measured by the camera, and W is the stored strain energy density, which can be identified from the measured nominal stress versus stretch curves of an unnotched sample at different stretches over cycles, i.e., $W(\lambda_a, N) = \int_1^{\lambda_a} S(N)d\lambda$. The unnotched sample shares the identical geometrical dimensions with the notched sample with a pre-existing crack. By varying the applied stretch of λ_{max}, we acquired the curve of crack extension per cycle dc/dN versus the applied energy release rate G. The fatigue threshold was obtained by linearly extrapolating the curve of dc/dNversus G to the intercept with the abscissa.

SEM imaging

The nanofibrous hydrogels in the dry state were sputter-coated with gold. The surfaces of nanofibrous hydrogels were imaged by a scanning electron microscope (JEOL 5910).

Confocal imaging

To visualize the microstructures of PVA nanofibrous hydrogels, a fluorescent dye, 5-([4,6-dichlorotriazin-2-yl]amino) fluorescein hydrochloride (5-DTAF), was used to label the hydroxyl groups in PVA.[33] Specifically, 1.0 mL of 0.5 wt% 5-DTAF in anhydrous dimethyl sulfoxide was added into 100 mL of sodium bicarbonate aqueous solution (0.1 M [pH 9.0]) to form a reactive dye solution. The PVA nanofibrous hydrogels were immersed in the dye solution for 12 h at 4°C in the dark to conjugate fluorochrome to PVA. Finally, the nanofibrous hydrogel samples were rinsed several times with water to wash away the non-conjugated dyes before fluorescence imaging. To achieve *in situ* fluorescent imaging of the nanofibrous hydrogels, the hydrogel samples were stretched under uniaxial tension using a linear stretcher (MicroVice

Holder, STJ-0116). The microstructures of nanofibrous hydrogel were imaged using a confocal microscope (Leica TCS SP8). Laser intensity, filter sensitivity, and gray-scale threshold were adjusted in each application to optimize the contrast of the images.

X-Ray scattering

The X-ray scattering measurement was performed on the nanofibrous hydrogel samples with a PILATUS3 R 300K detector in an X-ray scattering instrument (Bruker Nanostar). We used a wide-angle 2-mm beamstop with a sample-detector distance of 109.1 mm for wide-angle X-ray scattering (WAXS) measurements. The exposure time was set as 300 s. Raw WAXS patterns were processed with corrections by MATLAB-based GIXSGUI software before analysis.

Measurement of crystallinity

We measured the crystallinities of nanofibrous hydrogels using DSC (DSC/cell: RCS1-3277; cooling system: DSC1-0107).[25] In a typical crystallinity measurement, the sample was heated from 50°C to 250°C at a rate of 10°C/min under a nitrogen atmosphere with a flow rate of 30 mL/min. The integration of the endothermic transition ranging from 200°C to 250°C gives the enthalpy for melting the crystalline domains per unit mass of the dry sample $H_{crystalline}$. Therefore, the crystallinity of the sample can be calculated by $H_{crystalline}/H^0_{crystalline}$, where $H^0_{crystalline} = 138.6$ J/g is the enthalpy of fusion of 100 wt% crystalline PVA measured at the equilibrium melting point.[51]

Measurement of nanofiber volume fraction

We measured the mass m and volume V of one nanofibrous PVA sample in the dry state. The volume fraction of the nanofibers in the dry state was calculated by $m/(\rho_{PVA}V)$, where $\rho_{PVA} = 1.19$ g/cm^3 is the density of PVA polymers.

High-velocity microparticle impact experiment

Using the laser-induced particle impact test,[52] we conducted microparticle impact experiments to characterize the impact resistance of the bouligand-type nanofibrous hydrogels.[48] Steel microparticles (diameter: 17 $\pm$ 1 μm) were launched by a laser excitation pulse with varying intensities to reach different impact velocities. The velocities of the launched microparticles were measured using an ultrahigh-frame-rate camera yielding 16 frames (SIMX16, Specialized Imaging) and a synchronized quasi-cw laser imaging pulse for illumination (Cavilux, Specialized Imaging 640-nm wavelength, 10-μs duration). Depending on the impact velocity, the microparticles can perforate the film, be embedded in the film, or rebound. The specific energy penetration of the measured sample was determined by fitting the perforation data to find the ballistic limit v_{bl} using the Recht-Ipson model (details are provided in the supplemental information).[53] The specific energy of penetration is defined as the dissipated energy during perforation over the mass of sample affected by the impact, m_s, and can be directly related to the ballistic limit through $E_p = {}^1/_2\, M_p/m_s\, v_{bl}^2$, where M_p is the projectile mass. For simplicity, we assumed that the impact energy was absorbed by a plug of material whose cross-section equals the cross-section of the particle and whose length equals the sample thickness, as described in previous work.[48]

SUPPLEMENTAL INFORMATION

Supplemental information can be found online at https://doi.org/10.1016/j.matt.2021.03.023.

ACKNOWLEDGMENTS

The authors acknowledge the helpful comments from Dr. J.D. Joannopoulos. This work is supported by the U.S. Army Research Office through the Institute for Soldier Nanotechnologies at MIT (W911NF-13-D-0001) and Massachusetts Institute of Technology .

AUTHOR CONTRIBUTIONS

S.L., J.N., and X.Z. conceived the idea and designed the study. J.N. and X.L. prepared the sample. J.N. and S.L. conducted the mechanical and fatigue characterizations. Z.Q. performed the network simulations. D.V., Y.S., and J.N. conducted the impact particle tests whose application to this area was planned by K.A.N. and A.J.H. S.L. and J.N. conducted the structural characterizations using X-ray scattering, differential scanning calorimetry, scanning electron microscope, and confocal laser scanning microscopy. S.L., J.N., X.L., D.V., Y.S., R.R., K.A.N., A.J.H., and X.Z. analyzed and interpreted the result. S.L., J.N., X.L., and X.Z. wrote the manuscript with the inputs from all authors. X.Z. supervised the study.

DECLARATION OF INTERESTS

The authors declare no competing interests.

Received: January 25, 2021
Revised: March 18, 2021
Accepted: March 30, 2021
Published: April 23, 2021

REFERENCES

1. Nerurkar, N.L., Baker, B.M., Sen, S., Wible, E.E., Elliott, D.M., and Mauck, R.L. (2009). Nanofibrous biologic laminates replicate the form and function of the annulus fibrosus. Nat. Mat *8*, 986–992.
2. Homaeigohar, S., Disci-Zayed, D., Dai, T., and Elbahri, M. (2013). Biofunctionalized nanofibrous membranes mimicking carnivorous plants. Bioinspired, Biomim Nanobiomaterials *2*, 186–193.
3. Xue, J., Wu, T., Dai, Y., and Xia, Y. (2019). Electrospinning and electrospun nanofibers: methods, materials, and applications. Chem. Rev. *119*, 5298–5415.
4. Yang, Z., Wang, C., and Lu, X. (2019). Nanofibrous materials. In Electrospinning: Nanofabrication and Applications (Elsevier), pp. 53–92.
5. Zhang, X. (2018). Lipo-hydrogel Drug Carrier for Bone Regeneration (Elsevier).
6. Parada, G.A., and Zhao, X. (2018). In Ideal Reversible Polymer Networks, G. Sharma, ed. (Royal Society of Chemistry).
7. Xie, Z., Paras, C.B., Weng, H., Punnakitikashem, P., Su, L.-C., Vu, K., Tang, L., Yang, J., and Nguyen, K.T. (2013). Dual growth factor releasing multi-functional nanofibers for wound healing. Acta Biomater. *9*, 9351–9359.
8. Hadisi, Z., Farokhi, M., Bakhsheshi-Rad, H.R., Jahanshahi, M., Hasanpour, S., Pagan, E., Dolatshahi-Pirouz, A., Zhang, Y.S., Kundu, S.C., and Akbari, M. (2020). Hyaluronic acid (HA)-based silk fibroin/zinc oxide core–shell electrospun dressing for burn wound management. Macromol Biosci. *20*, 1900328.
9. Li, Z., Chu, D., Gao, Y., Jin, L., Zhang, X., Cui, W., and Li, J. (2019). Biomimicry, biomineralization, and bioregeneration of bone using advanced three-dimensional fibrous hydroxyapatite scaffold. Mater. Today Adv. *3*, 100014.
10. Lei, Z., Zhu, W., Zhang, X., Wang, X., and Wu, P. (2020). Bio-inspired ionic skin for theranostics. Adv. Funct. Mater. 2008020.
11. Leonhardt, E.E., Kang, N., Hamad, M.A., Wooley, K.L., and Elsabahy, M. (2019). Absorbable hemostatic hydrogels comprising composites of sacrificial templates and honeycomb-like nanofibrous mats of chitosan. Nat. Commun. *10*, 1–9.
12. Zhao, J., Kirillova, A., Kelly, C.N., Xu, H., Koshut, W.J., Yang, F., Gall, K., and Wiley, B.J. (2020). High-strength hydrogel attachment through nanofibrous reinforcement. Adv. Healthc. Mater. 2001119.
13. Nayeem, M.O.G., Lee, S., Jin, H., Matsuhisa, N., Jinno, H., Miyamoto, A., Yokota, T., and Someya, T. (2020). All-nanofiber–based, ultrasensitive, gas-permeable mechanoacoustic sensors for continuous long-term heart monitoring. Proc. Natl. Acad. Sci. U S A *117*, 7063–7070.
14. Kaltenbrunner, M., Sekitani, T., Reeder, J., Yokota, T., Kuribara, K., Tokuhara, T., Drack, M., Schwödiauer, R., Graz, I., and Bauer-Gogonea, S. (2013). An ultra-lightweight design for imperceptible plastic electronics. Nature *499*, 458–463.
15. Yuk, H., Lu, B., Lin, S., Qu, K., Xu, J., Luo, J., and Zhao, X. (2020). 3D printing of conducting polymers. Nat. Commun. *11*, 1–8.
16. Oh, D.X., Kim, S., Lee, D., and Hwang, D.S. (2015). Tunicate-mimetic nanofibrous hydrogel adhesive with improved wet adhesion. Acta Biomater. *20*, 104–112.
17. Yuk, H., Varela, C.E., Nabzdyk, C.S., Mao, X., Padera, R.F., Roche, E.T., and Zhao, X. (2019). Dry double-sided tape for adhesion of wet tissues and devices. Nature *575*, 169–174.
18. Higashi, K., and Miki, N. (2014). A self-swimming microbial robot using microfabricated nanofibrous hydrogel. Sens Actuat. B Chem. *202*, 301–306.
19. Zhou, Y., Yang, D., Chen, X., Xu, Q., Lu, F., and Nie, J. (2008). Electrospun water-soluble carboxyethyl chitosan/poly (vinyl alcohol) nanofibrous membrane as potential wound dressing for skin regeneration. Biomacromolecules *9*, 349–354.
20. Tonsomboon, K., Butcher, A.L., and Oyen, M.L. (2017). Strong and tough nanofibrous hydrogel composites based on biomimetic principles. Mater. Sci. Eng. C *72*, 220–227.
21. Wade, R.J., Bassin, E.J., Gramlich, W.M., and Burdick, J.A. (2015). Nanofibrous hydrogels with spatially patterned biochemical signals to

control cell behavior. Adv. Mater. *27*, 1356–1362.

22. Chen, J.-P., Chang, G.-Y., and Chen, J.-K. (2008). Electrospun collagen/chitosan nanofibrous membrane as wound dressing. Colloids Surf. A. Physicochem. Eng. Asp. *313*, 183–188.

23. Qin, X.H., and Wang, S.Y. (2008). Electrospun nanofibers from crosslinked poly(vinyl alcohol) and its filtration efficiency. J. Appl. Polym. Sci. *109*, 951–956.

24. Schoenmakers, D.C., Rowan, A.E., and Kouwer, P.H. (2018). Crosslinking of fibrous hydrogels. Nat. Commun. *9*, 1–8.

25. Lin, S., Liu, X., Liu, J., Yuk, H., Loh, H.-C., Parada, G.A., Settens, C., Song, J., Masic, A., and McKinley, G.H. (2019). Anti-fatigue-fracture hydrogels. Sci. Adv. *5*, eaau8528.

26. Ling, S., Kaplan, D.L., and Buehler, M.J. (2018). Nanofibrils in nature and materials engineering. Nat. Rev. Mater. *3*, 1–15.

27. Wu, J., Qin, Z., Qu, L., Zhang, H., Deng, F., and Guo, M. (2019). Natural hydrogel in American lobster: a soft armor with high toughness and strength. Acta Biomater. *88*, 102–110.

28. Taylor, D., O'Mara, N., Ryan, E., Takaza, M., and Simms, C. (2012). The fracture toughness of soft tissues. J. Mech. Behav. Biomed. Mater. *6*, 139–147.

29. Koski, A., Yim, K., and Shivkumar, S. (2004). Effect of molecular weight on fibrous PVA produced by electrospinning. Mater. Lett. *58*, 493–497.

30. Yang, F., Zhao, J., Koshut, W.J., Watt, J., Riboh, J.C., Gall, K., and Wiley, B.J. (2020). A synthetic hydrogel composite with the mechanical behavior and durability of cartilage. Adv. Funct. Mater. *30*, 2003451.

31. Hagiwara, Y., Putra, A., Kakugo, A., Furukawa, H., and Gong, J.P. (2010). Ligament-like tough double-network hydrogel based on bacterial cellulose. Cellulose *17*, 93–101.

32. Xu, H., Liu, Y., Xie, Y., Zhu, E., Shi, Z., Yang, Q., and Xiong, C. (2019). Doubly cross-linked nanocellulose hydrogels with excellent mechanical properties. Cellulose *26*, 8645–8654.

33. Lin, S., Liu, J., Liu, X., and Zhao, X. (2019). Muscle-like fatigue-resistant hydrogels by mechanical training. Proc. Natl. Acad. Sci. U S A *116*, 10244–10249.

34. Gent, A.N. (2012). Engineering with Rubber: How to Design Rubber Components (Carl Hanser Verlag GmbH Co KG).

35. Hamdi, A., Boulenouar, A., Benseddiq, N., and Guessasma, S. (2019). Crack propagation in elastomers subjected to cyclic loading. Proc. Inst. Mech. Eng. Pt. L. J. Mater. Des. Appl. *233*, 2301–2310.

36. Lake, G., and Thomas, A. (1967). The strength of highly elastic materials. Proc. Math. Phys. Eng. Sci. *300*, 108–119.

37. Akagi, Y., Sakurai, H., Gong, J.P., Chung, U.-i., and Sakai, T. (2013). Fracture energy of polymer gels with controlled network structures. Int. J. Chem. Phys. *139*, 144905.

38. Koosha, M., and Mirzadeh, H. (2015). Electrospinning, mechanical properties, and cell behavior study of chitosan/PVA nanofibers. J. Biomed. Mater. Res. A *103*, 3081–3093.

39. Zhang, Y., Venugopal, J., Huang, Z.-M., Lim, C.T., and Ramakrishna, S. (2006). Crosslinking of the electrospun gelatin nanofibers. Polymer *47*, 2911–2917.

40. Huang, Z.-M., Zhang, Y., Ramakrishna, S., and Lim, C. (2004). Electrospinning and mechanical characterization of gelatin nanofibers. Polymer *45*, 5361–5368.

41. Nguyen, T.-H., and Lee, B.-T. (2010). Fabrication and characterization of cross-linked gelatin electro-spun nano-fibers. J. Biomed. Eng. *3*, 1117.

42. Butcher, A.L., Koh, C.T., and Oyen, M.L. (2017). Systematic mechanical evaluation of electrospun gelatin meshes. J. Mech. Behav. Biomed. Mater. *69*, 412–419.

43. De Silva, R.T., Dissanayake, R.K., Mantilaka, M.P.G., Wijesinghe, W.S.L., Kaleel, S.S., Premachandra, T.N., Weerasinghe, L., Amaratunga, G.A., and de Silva, K.N. (2018). Drug-loaded halloysite nanotube-reinforced electrospun alginate-based nanofibrous scaffolds with sustained antimicrobial protection. ACS Appl. Mater. Interfaces *10*, 33913–33922.

44. Hansen, L.M., Smith, D.J., Reneker, D.H., and Kataphinan, W. (2005). Water absorption and mechanical properties of electrospun structured hydrogels. J. Appl. Polym. Sci. *95*, 427–434.

45. Illeperuma, W.R., Sun, J.-Y., Suo, Z., and Vlassak, J.J. (2014). Fiber-reinforced tough hydrogels. Extreme Mech. Lett. *1*, 90–96.

46. He, Q., Wang, Z., Yan, Y., Zheng, J., and Cai, S. (2016). Polymer nanofiber reinforced double network gel composite: strong, tough and transparent. Extreme Mech. Lett. *9*, 165–170.

47. Fabritius, H., Sachs, C., Raabe, D., Nikolov, S., Friák, M., and Neugebauer, J. (2011). Chitin in the exoskeletons of arthropoda: from ancient design to novel materials science. In Chitin (Springer), pp. 35–60.

48. Veysset, D., Sun, Y., Kooi, S.E., Lem, J., and Nelson, K.A. (2020). Laser-driven high-velocity microparticle launcher in atmosphere and under vacuum. Int. J. Impact Eng. *137*, 103465.

49. Qin, Z., and Buehler, M.J. (2011). Flaw tolerance of nuclear intermediate filament lamina under extreme mechanical deformation. ACS Nano *5*, 3034–3042.

50. Plimpton, S. (1995). Fast parallel algorithms for short-range molecular dynamics. J. Comput. Phys. *117*, 1–19.

51. Peppas, N.A., and Merrill, E.W. (1976). Differential scanning calorimetry of crystallized PVA hydrogels. J. Appl. Polym. Sci. *20*, 1457–1465.

52. Veysset, D., Hsieh, A.J., Kooi, S., Maznev, A.A., Masser, K.A., and Nelson, K.A. (2016). Dynamics of supersonic microparticle impact on elastomers revealed by real–time multi–frame imaging. Sci. Rep. *6*, https://doi.org/10.1038/srep25577.

53. Recht, R., and Ipson, T. (1963). Ballistic perforation dynamics. J. Appl. Mech. *30*, 384–390.

Supplemental Information for

Strong Fatigue-Resistant Nanofibrous Hydrogels Inspired by Lobster Underbelly

Jiahua Ni[1,9], Shaoting Lin[1,9], Zhao Qin[2,9], David Veysset[3,4,5], Xinyue Liu[1], Yuchen Sun[3,4], Alex J. Hsieh[6], Raul Radovitzky[3,7], Keith A. Nelson[3,4], Xuanhe Zhao[1,3,8]*

[1]Department of Mechanical Engineering, Massachusetts Institute of Technology, Cambridge, MA 02139, USA

[2]Department of Civil and Environmental Engineering, Syracuse University, Syracuse, NY, 13244, USA

[3]Institute for Soldier Nanotechnologies, Massachusetts Institute of Technology, Cambridge, MA 02139, USA

[4]Department of Chemistry, Massachusetts Institute of Technology, Cambridge, MA 02139, USA

[5]Hansen Experimental Physics Laboratory, Stanford University, Stanford, CA 94305

[6]U.S. Army Combat Capabilities Development Command, Army Research Laboratory, RDRL-WMM-G, Aberdeen Proving Ground, MD 21005-5069, USA

[7]Department of Aeronautics and Astronautics, Massachusetts Institute of Technology, Cambridge, MA 02139, USA

[8]Department of Civil and Environmental Engineering, Massachusetts Institute of Technology, Cambridge, MA 02139, USA

[9]Jiahua Ni, Shaoting Lin, Zhao Qin contributed equally to this work.

*Correspondence: zhaox@mit.edu

Modeling of deformation of nanofibrous networks

The network is modeled by the assembly of 673 non-crosslinked nanofibers (composed of 98,586 coarse-grained beads in total) with each of them explicitly modeled by a coarse-grained bead-spring model in a simulation box of 500×500×200 (*x* by *y* by *z*) μm^3 with periodic condition in all the three directions. By keeping the dimension of the box constant in *x* and *y* directions, we apply an external pressure of 100 MPa to the simulation box during an energy minimization in *z* direction. The energy minimization of 10,000 steps is followed by a dynamics run in a NVT (constant particle number, volume and room temperature) ensemble with a time step of 0.1 μs and total steps of 2,000. We repeat this minimization-dynamics process for 100 cycles to ensure the box is fully compressed in LAMMPS. After this, we relax the *z* dimension to 97 μm, allowing the fibers to get compressed together and get the contact at the cross point. We write a Matlab script to compute the distance between any pair of beads within any pair of the nanofibers. We modify the bond list by adding a crosslink bond if any two beads within two individual fibers are within 1.5 μm, which enables us to connect all the fibers to form an integrated network. We systematically change the interfacial interaction between two nanofibers in contact by tuning the stress-strain curve of the interfacial material according to **Equation 2** in the main paper. Using the NVT ensemble, we apply deformation to the network by deforming the entire simulation box and remap the coordinate of all the beads in the *x* direction. The strain rate of 100 /s is applied for each time step. To prevent the network from relaxing during the deformation, we fix all the beads within a rectangular region of 20 μm in width on each side by removing them from the integration step during the dynamics run. The total force on each side of the network during loading is obtained by summing up the atomic force on all the beads in each region. Because the thickness of the network in the simulation box is not quite uniform because of its limited thickness and increasing the thickness can significantly increase the simulation time, we use the density of the polymer network in the experiment to define the model thickness. In experiment, the 3D polymer content is ~20% as ρ_{3D}=0.2 m^3/m^3. In the simulation model,

the 2D polymer content is given by $\rho_{2D} = N\frac{\pi r_0 d^2}{4}/(l_x \cdot l_x) = 3.10 \times 10^{-7}$ m^3/m^2, we thus define the mean thickness of the simulation model as t=ρ_{2D}/ρ_{3D}=1.55 μm for stress calculation.

The nominal stress (σ_{fiber}) versus nominal strain (ε) curve of each fiber is modelled by a tri-section potential

$$\sigma_{\text{fiber}}(\varepsilon) = \left[\exp\left(\frac{\varepsilon-\varepsilon_b}{1+\varepsilon_b}\Xi\right)+1\right]^{-1}\begin{cases} E_1\varepsilon & \varepsilon < \varepsilon_1 \\ H_\varphi(\varepsilon) & \varepsilon_1 \le \varepsilon < \varepsilon_2 \\ R_2 + E_2(\varepsilon-\varepsilon_2) & \varepsilon_2 \le \varepsilon \end{cases} \quad \text{(Equation S1)}$$

In **Equation S1**, E_i and ε_i are spring constants that are derived directly from the force-extension curve of the experimental tensile test of the PVA nanofiber at different regions, as E_1 is the Young's modulus of the thread. The Fermi–Dirac distribution function introduces two additional parameters ε_b and Ξ. [1,2] The parameter ε_b denotes the critical strain for breaking of the filament and the parameter Ξ describes the amount of smoothing around the breaking point (the smaller Ξ, the smoother the curve becomes). The parameters $R_1 = H_\varphi(\varepsilon_1) = E_1\varepsilon_1$ and R_2 are calculated from force continuity conditions. H_φ is the Hermite interpolation function that is used to smoothly connect the two linear curves [3], which is defined as:

$$H_\varphi(\varepsilon) = (m_1\varepsilon + n_1)\left(\frac{\varepsilon-\varepsilon_2}{\varepsilon_1-\varepsilon_2}\right)^2 + (m_2\varepsilon + n_2)\left(\frac{\varepsilon-\varepsilon_1}{\varepsilon_2-\varepsilon_1}\right)^2 \quad \text{(Equation S2)}$$

where m_i, n_i are coefficients determined by the connectivity conditions as $H_\varphi(\varepsilon_1) = R_1$, $H_\varphi(\varepsilon_2) = R_2$, $H_\varphi'(\varepsilon_1) = E_1$ and $H_\varphi'(\varepsilon_2) = E_2$ and hence their values are given by

$$\begin{cases} m_1 = E_1 - 2\frac{R_1}{\varepsilon_1-\varepsilon_2} \\ n_1 = R_1 - (E_1 - 2\frac{R_1}{\varepsilon_1-\varepsilon_2})\varepsilon_1 \\ m_2 = E_2 - 2\frac{R_2}{\varepsilon_2-\varepsilon_1} \\ n_2 = R_2 - (E_2 - 2\frac{R_2}{\varepsilon_2-\varepsilon_1})\varepsilon_2 \end{cases} \quad \text{(Equation S3)}$$

The bending stiffness of the thread is reflected by the angular spring between two neighbouring springs that defines the bending stiffness of the thread, and its numerical value is given by

$$K_B = E_1 I_t/(2r_0) = E_1 \pi d^4/(128 r_0) \quad \text{(Equation S4)}$$

The bending energy of each angular spring is $\varphi_B(\theta) = K_B(\theta - \pi)^2$, where θ is the angle between two neighbouring springs. By carefully design the force-extension function and the parameters of the nonlinear spring, this model can very well reproduce the experimental measurement of a single fiber (**Figure S4**). All the numerical values of the parameters for PVA nanofiber are summarized in **Table S1**.

Fatigue characterization of a single nanofiber

Existing methods for measuring mechanical properties of a single nanofiber typically rely on a three-point bending test by atomic force microscope (AFM)[4] or a uniaxial tensile test using nano tester.[5] However, most of these methods still face challenges for measuring the mechanical properties of a hydrogel nanofiber in the hydrated state due to the uncontrollable dehydration during the measurement. The force level for a hydrogel nanofiber with a diameter of 1000 nm is on the order of 1 μN, lower than the measurable force of a typical nano tester. Moreover, none of these methods have been adopted to measure the mechanical properties of a single nanofiber under multiple cycles of load. Here, we propose a new method to characterize the fatigue properties of a single fiber. Instead of applying load on a single fiber, we apply mechanical load on a fibrous film which contains a bundle of aligned continuous long fibers. This method shows several benefits. First and foremost, the force level can be highly amplified for high-resolution measurements. Secondly, the aligned fibrous film can be immersed in a water bath for the equilibrium swollen state. Lastly, common mechanical tester can be readily used to apply cyclic loading on the aligned nanofibrous film for fatigue characterization.

We first fabricate aligned fibrous PVA films by ejecting charged threads of PVA polymer solution on a rotating cylinder collector. We specifically set the rotation speed as 1000 rpm such that the linear velocity of the rotating cylindrical surfaces matches that of the ejected polymer threads. The SEM image in **Figure S7B** verifies the aligned fibrous structure in the film. The aligned fibrous film is further transferred into a water bath for hydration and swelling, and thereafter subjected to mechanical loading

for fatigue characterization (**Figure S7**). We first characterize the engineering stress versus stretch curve of the aligned fibrous film under a single cycle of uniaxial loading. With the measured porosity of the film in the dry state ϕ, the corresponding stress (i.e., S) versus stretch (i.e., λ) for a single fiber can be calculated by

$$S = \frac{F}{A\Phi Q_t Q_{plane}} \quad \text{(Equation S5)}$$

where F is the measured force applied on the film, A is the cross-sectional area of the film at undeformed dry state, and $\Phi = 1 - \phi$ is the polymer volume fraction of the film in the dry state (i.e., 50 %), Q_t is the swelling ratio along the thickness direction (i.e., 1.77), and Q_{plane} is the swelling ratio along the in-plane directions (i.e., 1.05), as shown in **Figure S6**. **Figures S7C** and **S7D** plot the measured stress versus stretch curve of a single fiber in the swollen state, which shows the identical Young's modulus and stress versus stretch curve at relatively small deformations (stretch below 3) for the films with different lengths. However, the ultimate tensile strength varies significantly for films with different lengths (**Figure S7E**). For the film with a length of 25 mm, the measured fibril strength is only 17 MPa (**Figures S7D** and **S7E**). As the film length decreases, the fiber strength gradually increases up to 28 MPa and maintains constant. This result reveals that the measured fiber strength is highly sensitive to the sample length if the sample length is much greater than the length of a single fiber, because such a long sample tends to fail by fracturing the interface between adjacent fibers instead of fracturing the fibers. Instead, if the sample length is smaller than that of a single fiber, the measured fiber strength should approach the ideal nominal strength of a single fiber (i.e., $S_{fiber} = 28\,\text{MPa}$), which is independent of the sample length.

We further apply cyclic loading on the film under constant maximum stress of S_a below the measured strength of a single fiber (i.e., $S_a = 25.5\,\text{MPa}$, $S_{fiber} = 28\,\text{MPa}$), recording the stretch applied on the film (**Figures S8B** and **S8C**). The maximum stretch applied on the film gradually increases due

to the plastic deformation accumulated in the fibers under such dynamic creep loading. The film eventually breaks as the cycle number reaches a critical value (i.e., $N_c = 496$ for $S_a = 25.5\,\text{MPa}$). **Figure S9B** summarizes the critical cycle number N_c as a function of applied maximum stress S_a. It is notable that the critical cycle number increases dramatically as the applied maximum stress decreases and there exists a critical maximum stress of S_a, below which the sample does not fail under repeated cycles of loading. We take the critical stress as the strength limit of a single fiber that can sustain under repeated cycles of loading, i.e., $S_L = 16.3\,\text{MPa}$. Unlike the case when the applied maximum stress is slightly lower than the strength of a single fiber (e.g., $S_a = 25.5\,\text{MPa} < S_{fiber} = 28\,\text{MPa}$), the maximum applied stretch gradually increases and maintains a plateau when the applied maximum stress is equal to the strength threshold (i.e., $S_a = 16.3\,\text{MPa}$) as shown in **Figure S8E**. We further calculate the stored elastic energy in a single fibril W over cycles by integrating the area of stress versus stretch curve over cycles at $S_a = S_L$,

$$W(N) = \int_1^{\lambda} S(S_a = S_L, N)\, d\lambda \qquad \text{(Equation S6)}$$

As shown in **Figure S9C**, the stored elastic energy under the 1st cycle of loading can reach as high as $1.3 \times 10^7\,\text{J/m}^3$, but decreases over cycles and maintains a steady-state value of $4.8 \times 10^6\,\text{J/m}^3$. We take the steady-state value of the stored elastic energy of a single fiber at $S_a = S_L$ as the strain energy limit of a single fiber (i.e., $W_L = 4.8\,\text{MJ/m}^3$) that can sustain multiple cycles of load with no fatigue failures.

Determination of specific impact penetration energy

We follow the analysis described by Veysset et al. to determine the specific penetration energies of the films [6]. We define the impact (incident) velocity of the projectile as v_i, the mass of the projectile as M_p, and the residual projectile velocity as v_r, with $v_r < 0$ for rebound and $v_r > 0$ for perforation (see **Figure**

6H). The residual velocity is zero in case of particle embedment. For perforation cases, we assume that the projectile punches a mass of sample, corresponding to the mass of material encountered by the projectile during perforation through the film thickness h and with a cross-section equals the projectile's cross-section A_p. We further assume that the mass of the plug hence ejected, $m_s = \rho_{sample} h A_p$, travels with the same velocity as the projectile, v_r. Thus, the conservation of energy yields:

$$\frac{1}{2} M_p v_i^2 = \frac{1}{2}\left(M_p + m_s\right) v_r^2 + W \qquad \text{(Equation S7)}$$

where W is the energy loss due to film deformation, heating, and failure. This energy can be directly found at the impact velocity threshold, in other words the ballistic limit v_{bl}, where $v_r = 0$

$$W = \frac{1}{2} M_p v_{bl}^2 \qquad \text{(Equation S8)}$$

We define the specific penetration energy, E_p, as W over the mass of sample affected by the impact, m_s. The residual velocity and the specific penetration energy can be rewritten as

$$v_r = \sqrt{\frac{M_p}{M_p + m_s}\left(v_i^2 - v_{bl}^2\right)} \qquad \text{(Equation S9)}$$

and

$$E_p = \frac{1}{2}\frac{M_p}{m_s} v_{bl}^2 \qquad \text{(Equation S10)}$$

We fit the perforation data (**Figure 6H**) to find the ballistic limit. We find the specific penetration energy for the dry state to be 70±10 kJ/kg and for the hydrated state to be 40±5 kJ/kg, which is on the same order of magnitude as what was found for polyethylene but about half.

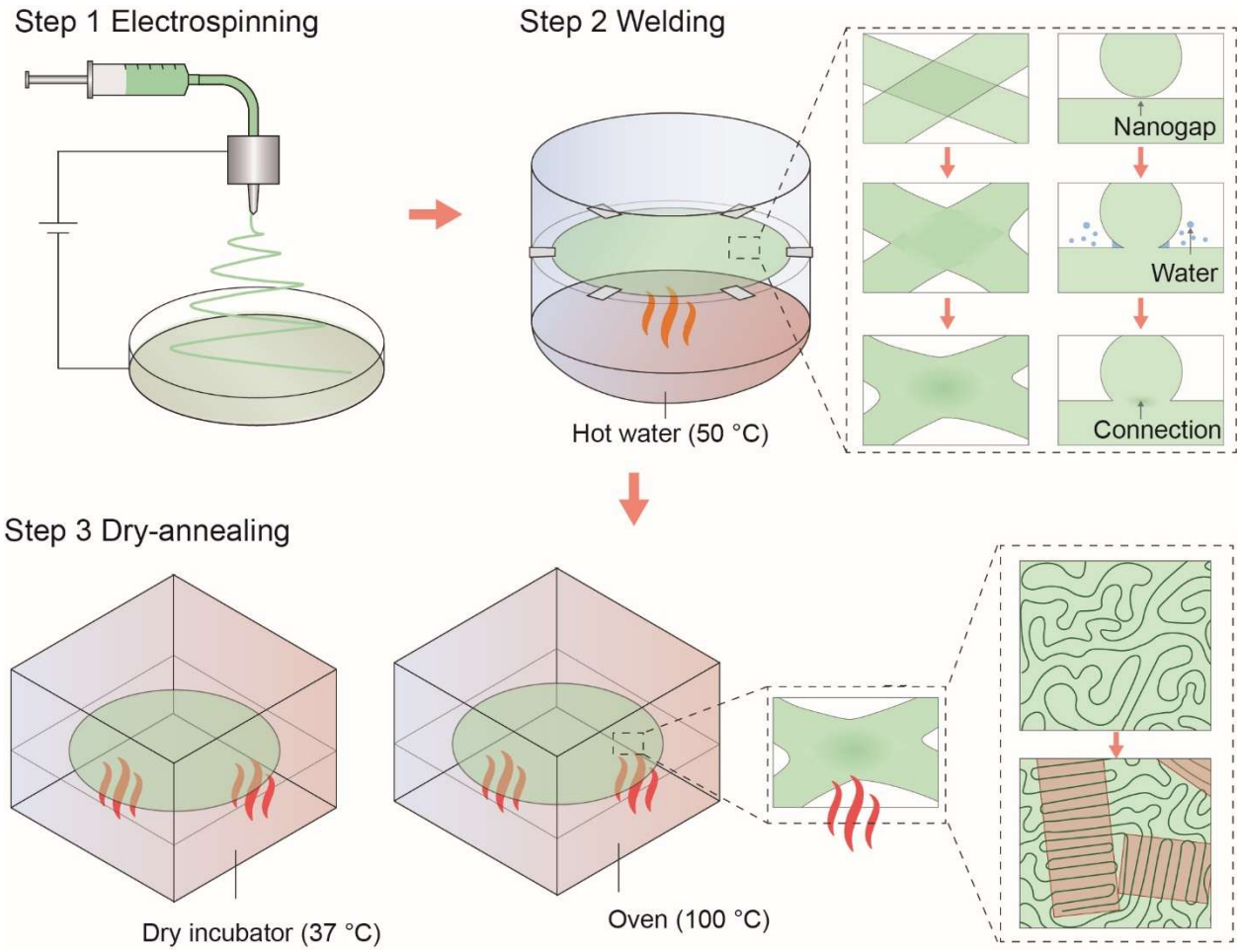

Figure S1. Schematic illustration of the fabrication process of electrospinning, welding, and dry-annealing.

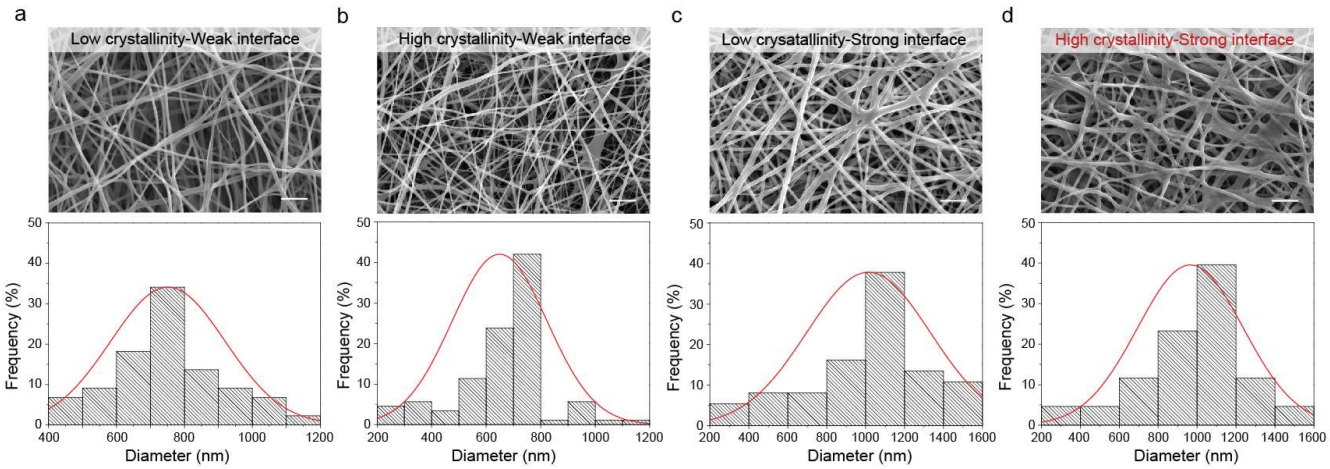

Figure S2. Histogram of nanofiber diameters from SEM images for various nanofibrous hydrogels with (A) Low crystallinity and weak interface, (B) How crystallinity and weak interface, (C) Low crystallinity and strong interface, and (D) High crystallinity and strong interface. The scale bars in the SEM images are 10 μm.

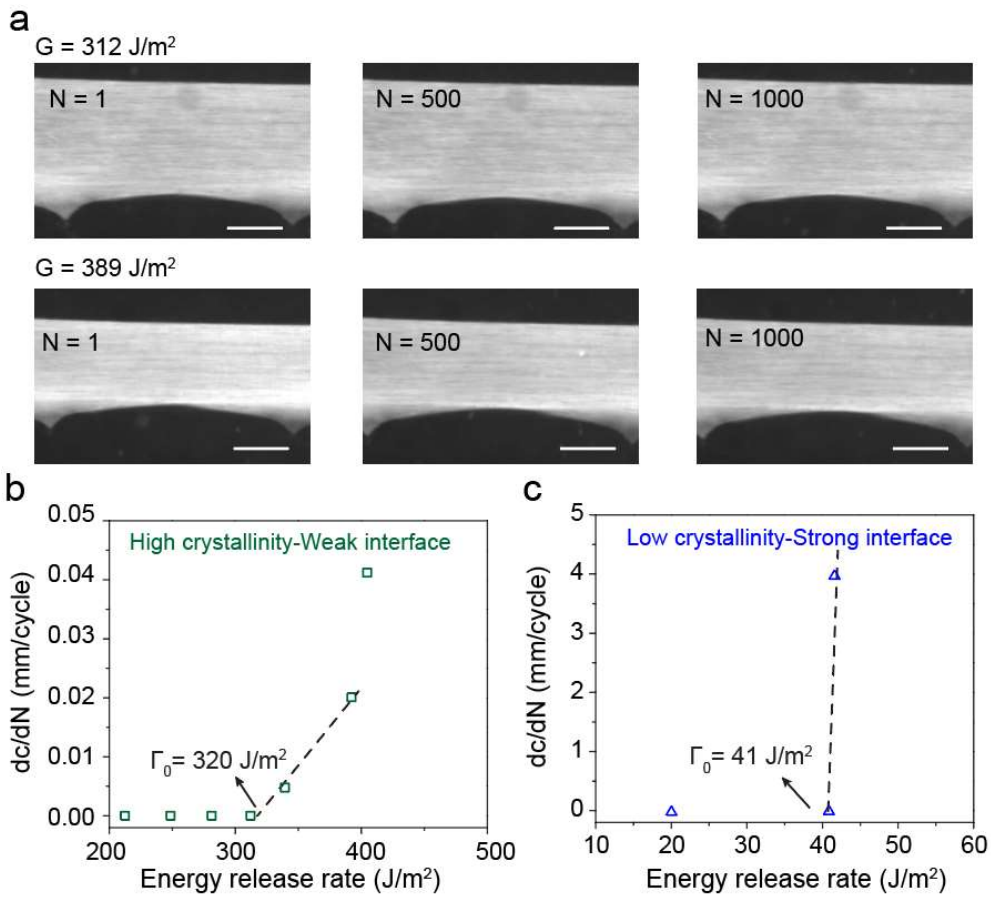

Figure S3. Fatigue characterizations of nanofibrous hydrogels. (A) Representative images of the notched nanofibrous hydrogels (i.e., high crystallinity-weak interface) under the applied energy release rate of 312 and 389 J/m^2 at the cycle numbers of 1, 500, and 1000. (B) Fatigue crack extension rate versus energy release curve of the nanofibrous hydrogels with high crystallinity and weak interface. (C) Fatigue crack extension rate versus energy release curve of the nanofibrous hydrogels with low crystallinity and strong interface. The scale bars in (A) are 1 mm.

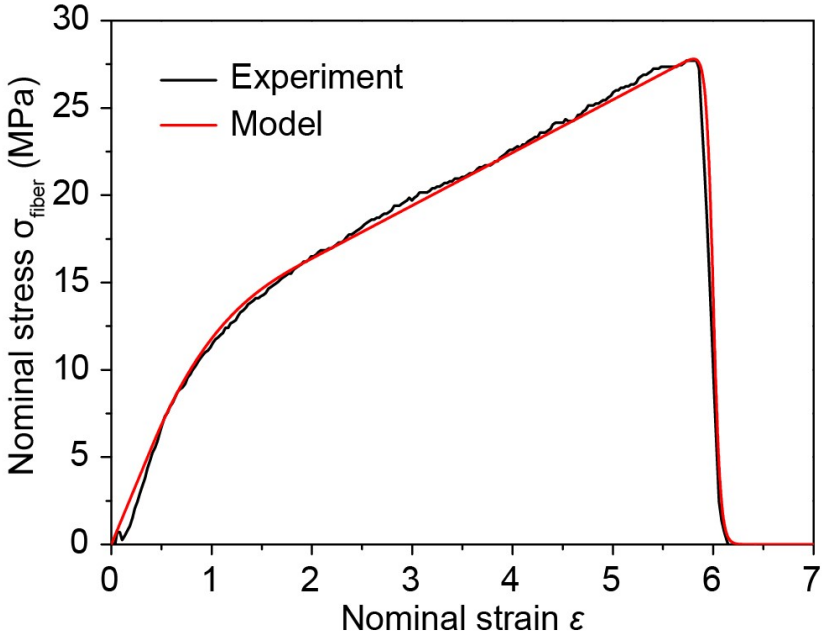

Figure S4. Nominal stress versus nominal strain curve of a single nanofiber. The fitted nominal stress versus nominal strain curve of a single fiber using the model in Equations S1-S4 to reproduce the experimental measured curve.

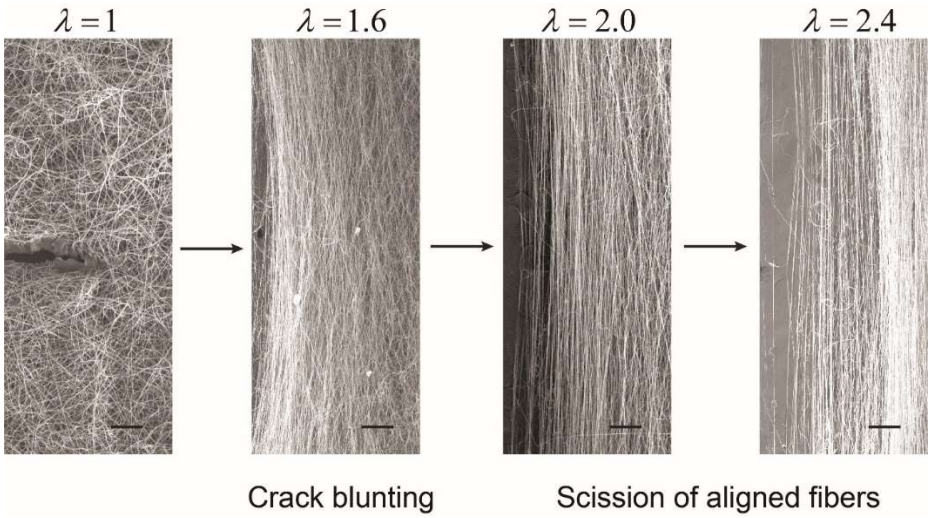

Figure S5. SEM images of the crack tip of a nanofibrous hydrogel with high crystallinity and strong interface at different stretch levels. The crack tip displays significant blunting followed by the scission of aligned primary fibers at the crack path. The scale bars are 100 μm.

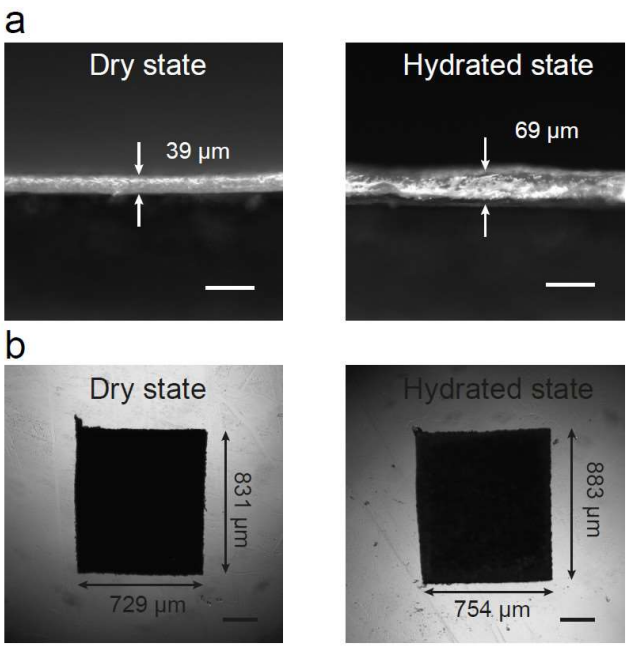

Figure S6. Measurement of the swelling ratio of the fatigue-resistant nanofibrous hydrogel. (A) $Q_t = 1.77$ along thickness direction and (B) $Q_{plane} = 1.05$ along in-plane directions. The scale bars in (A) and (B) are 200 μm.

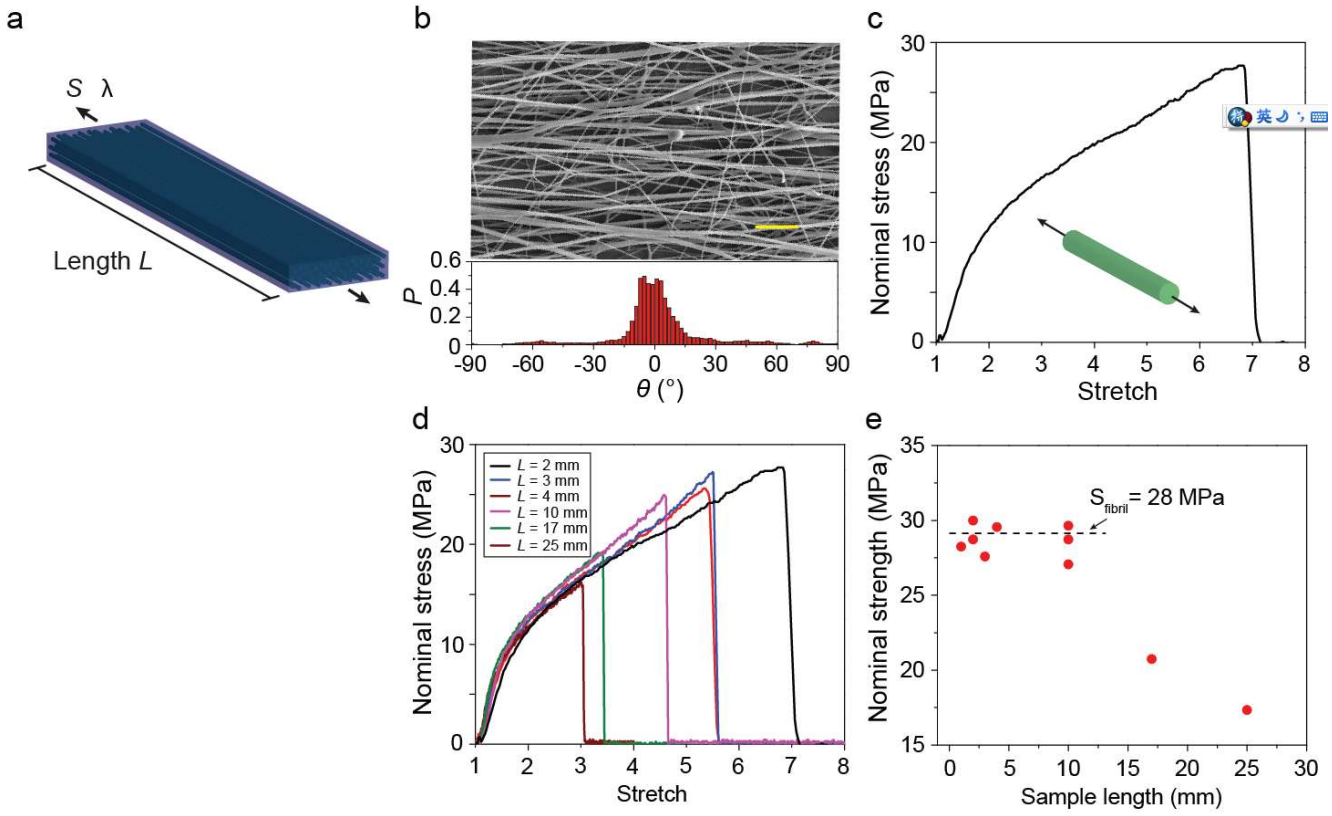

Figure S7. Mechanical characterization of a single nanofiber. (A) Schematic illustration of a uniaxial tensile test in a water bath. (B) The SEM image of the nanofibrous hydrogel with aligned fibers and corresponding histogram of the orientation of the aligned fibers. (C) Engineering stress versus stretch curve of a single nanofiber measured from the sample with the length of 2 mm. (D) Engineering stress versus stretch of the samples with different lengths. (E) Summarized nominal strengths of fibers versus the sample length. The scale bar in (B) is 10 μm.

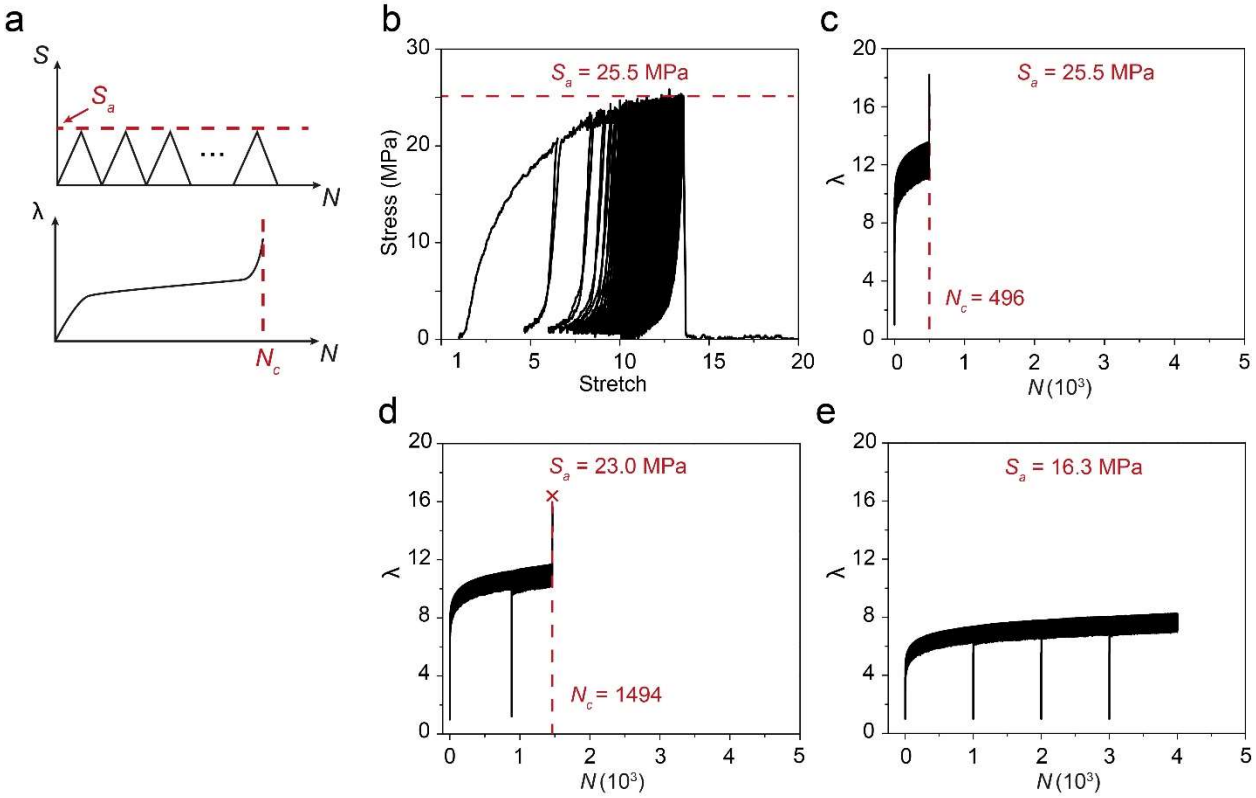

Figure S8. Fatigue characterization of a single nanofiber. (A) Schematic illustration of performing cyclic tensile loading on the sample with a constant maximum stress of S_a and measuring the stretch applied on the sample λ. (B) Engineering stress versus stretch under cyclic loading with a constant maximum stress of 25.5 MPa (i.e., $S_a = 25.5\,\text{MPa}$). (C-E) Measured stretch applied on the sample versus cycle number under cyclic loading (C) with a constant maximum stress of 25.5 MPa (i.e., $S_a = 25.5\,\text{MPa}$), (D) with a constant maximum stress of 23 MPa (i.e., $S_a = 23\,\text{MPa}$), and (E) with a constant maximum stress of 16.3 MPa (i.e., $S_a = 16.3\,\text{MPa}$).

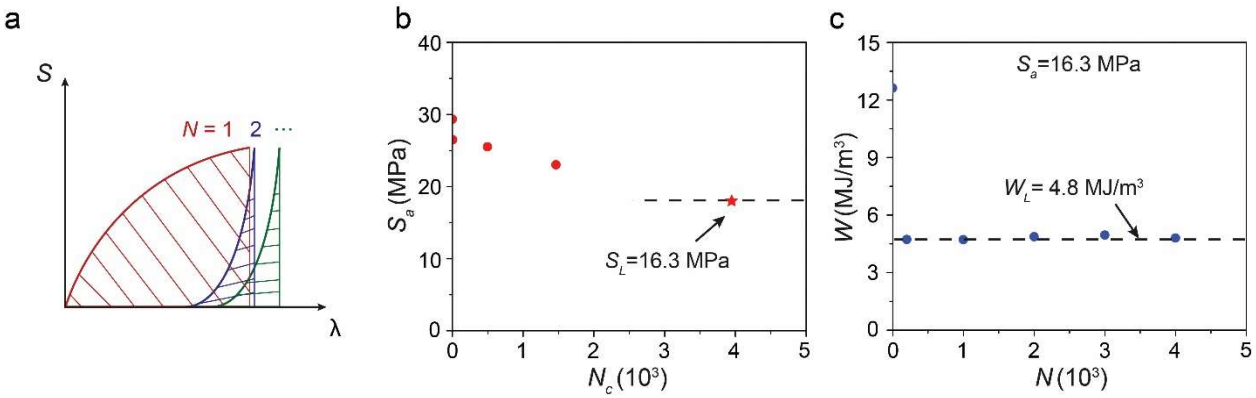

Figure S9. Measurement of the strain energy limit of a nanofiber. (A) Schematic illustration of calculating the elastic energy density per volume of the sample under cyclic loading with a constant maximum stress. (B) The critical cycle number N_c that a sample can sustain before fracture under cyclic loading with a constant maximum stress S_a. The strength limit of a nanofiber is identified as 16.3 MPa. (C) The elastic energy density of a single fiber W versus cycle number N under cyclic loading with a constant maximum stress of the strength limit (i.e., $S_a = S_L = 16.3\,\text{MPa}$). The strain energy limit of a nanofiber is identified as 4.8 MJ/m^3.

Table S1. Parameters for modeling the mechanics of coarse-grained nanofibers.

Parameter and units	Numerical value
Initial modulus E_1 (MPa)	13.84
Yielding modulus E_2 (MPa)	3.03
Critical strain ε_1, ε_2	0.4, 2.0
Rupture strain ε_b	6.0
Force continuity conditions R_1, R_2 (MPa)	5.536, 16.38
Hermite interpolation parameters m_1, m_2 (MPa)	20.76, -17.445
Hermite interpolation parameters n_1, n_2 (MPa)	-2.768, 51.27
Initial bond length r_0 (m)	1×10^{-6}
Equilibrium angle θ_0 (rad)	π
Bending stiffness parameter K_B (Nm/rad^2)	3.4×10^{-13}
Mass of each mesoscale particle M_{thread} (kg)	1.02×10^{-15}
Switch function Ξ	200
Length constant of nonbonding interaction r_c (μm)	1
Energy constant of nonbonding interaction α (J)	3×10^{-9}

References

1. Qin, Z., and Buehler, M.J. (2011). Flaw tolerance of nuclear intermediate filament lamina under extreme mechanical deformation. ACS Nano *5*, 3034-3042.

2. Wu, J., Qin, Z., Qu, L., Zhang, H., Deng, F., and Guo, M. (2019). Natural hydrogel in American lobster: a soft armor with high toughness and strength. Acta Biomater *88*, 102-110.

3. Spitzbart, A. (1960). A generalization of Hermite's interpolation formula. Am Math Mon *67*, 42-46.

4. Zhou, J., Cai, Q., Liu, X., Ding, Y., and Xu, F. (2018). Temperature Effect on the Mechanical Properties of Electrospun PU Nanofibers. Nanoscale Res Lett *13*, 1-5.

5. Tan, E., Ng, S., and Lim, C. (2005). Tensile testing of a single ultrafine polymeric fiber. Biomaterials *26*, 1453-1456.

6. Veysset, D., Sun, Y., Kooi, S.E., Lem, J., and Nelson, K.A. (2020). Laser-driven high-velocity microparticle launcher in atmosphere and under vacuum. Int J Impact Eng *137*, 103465.